

Analytical nonadiabatic couplings and gradients within the state-averaged orbital-optimized variational quantum eigensolver

Saad Yalouz,^{1,2,*} Emiel Koridon,^{1,*} Bruno Senjean,^{3,†} Benjamin Lasorne,^{3,‡} Francesco Buda,⁴ and Lucas Visscher¹

¹*Theoretical Chemistry, Vrije Universiteit, De Boelelaan 1083, NL-1081 HV, Amsterdam, The Netherlands*

²*Instituut-Lorentz, Universiteit Leiden, P.O. Box 9506, 2300 RA Leiden, The Netherlands*

³*ICGM, Univ Montpellier, CNRS, ENSCM, Montpellier, France*

⁴*Leiden Institute of Chemistry, Leiden University, Einsteinweg 55, P.O. Box 9502, 2300 RA Leiden, The Netherlands.*

In Ref. [1], we introduced the original idea of a hybrid quantum-classical algorithm, so-called state-averaged orbital-optimized variational quantum eigensolver (SA-OO-VQE), able to treat several electronic states on an equal footing based on the combination of two main algorithms: (1) a state-averaged orbital-optimizer, and (2) a state-averaged VQE. In this work, we pursue the development of our previous paper by introducing several technical and analytical extensions to the SA-OO-VQE method. Motivated by the limitations of current quantum computers, the first extension consists in an efficient state-resolution procedure to find the SA-OO-VQE eigenstates, and not just the subspace spanned by them, while remaining in the equi-ensemble framework. This approach avoids expensive intermediate resolutions of the eigenstates by postponing this problem to the very end of the full algorithm. The second extension allows for the estimation of analytical gradients and nonadiabatic couplings, which are crucial in many practical situations ranging from the search of conical intersections to the simulation of quantum dynamics, in, for example, photoisomerization reactions. The accuracy of our new implementations is demonstrated on the formaldehyde molecule CH_2NH (a minimal Schiff base model relevant for the study of photoisomerization in larger biomolecules), for which we also perform a geometry optimization to locate a conical intersection between the ground and first-excited electronic states of the molecule.

I. INTRODUCTION

Many fundamental processes in nature, such as photosynthesis and vision, are triggered by light absorption. Thus, a proper description of the associated primary light-induced photochemical events requires a quantum-mechanical approach able to treat accurately both the ground and the excited electronic states. Although density functional theory (DFT) and its time-dependent extension to excited states (TDDFT) have seen huge progress in treating molecular and condensed matter systems near equilibrium [2–4], these approaches are not adequate to accurately describe photochemical reaction paths where the Born-Oppenheimer approximation breaks down for several strongly coupled electronic states that get very close in energy [5]. Especially couplings between the first excited and ground states are problematic because of the single-reference character of many quantum chemical methods (for instance the popular time-dependent density functional theory, TDDFT approach). While single-reference approaches with spin-flip excitations might help to overcome some of these limitations [6], in general more accurate and computationally demanding multi-configurational wavefunction approaches are required for modeling these intrinsically nonadiabatic cases. A good example is the description of the prototypical photoisomerization process in the reti-

nal chromophore of rhodopsin, one of the most studied events in photobiology [7]. Schematically, after the initial photoexcitation, this event proceeds via the relaxation in the first excited state (S_1) towards a conical intersection (CoIn) region. Here, the population is transferred back to the ground state (S_0) where the isomerization is completed. In order to describe dynamically this type of event, one needs the knowledge of the potential energy surfaces (PES) for the electronic states involved in the process, typically S_0 and S_1 . Moreover, one should also efficiently compute the gradient of the PES with respect to the nuclear displacement, which in a semiclassical nonadiabatic molecular dynamics scheme provides the forces driving the nuclear subsystem [5, 7, 8]. Finally, it is also crucial to estimate the nonadiabatic coupling terms between the two electronic states, which eventually determine the conical topography of the crossing between the two PES and the dynamical coupling that results in population transfer between the two states [9, 10]. The challenge in computational quantum chemistry is to obtain all these necessary ingredients at an affordable numerical cost and yet with good accuracy.

Methods that are able to provide both nonadiabatic couplings and a correct description of the PES topology and topography (double cone of dimension two with respect to variations of the nuclear coordinates) of conical intersections require, formally, that the problem be solved at the very end with a final Hamiltonian diagonalization. When the crossing occurs between the first excited and ground states, this implies a democratic treatment of both wavefunctions within a common Slater determinant basis set, which in practice calls for a state-

* yalouzaad@gmail.com

† bruno.senjean@umontpellier.fr

‡ benjamin.lasorne@umontpellier.fr

averaged (SA) orbital optimization. This can be achieved in-principle by the state-averaged multiconfigurational self-consistent field (SA-MCSCF) method [11]. In practice, the diagonalization step is the principal bottleneck and one has to consider small complete active spaces (CAS), thus leading to the state-averaged complete active space self-consistent field (SA-CASSCF) method [11]. However, this decrease in complexity comes at the expense of a missing dynamical correlation treatment, that is usually recovered by multireference quasidegenerate perturbation techniques, as in the XMS-CASPT2 [12], XMCQDPT2 [13], or QD-NEVPT2 methods [14, 15]; see also Ref. [16] for a comparative discussion of the correct treatment of degeneracies with a selection of excited-state approaches.

With the advent of quantum computing, the dream of a very large CAS becomes possible again, thus turning small SA-CASSCF into large SA-CASSCF which should be good enough to account for a qualitatively correct description of the wave function and also include a substantial part of the (previously missing) so-called dynamical correlation. Recently, the *quantum analog* of SA-CASSCF has been introduced by Yalouz *et al.* [1] based on a state-averaged orbital-optimized (SA-OO) extension of the variational quantum eigensolver (VQE) algorithm [17, 18], thus referred to as the SA-OO-VQE algorithm. While SA-OO-VQE has been shown to provide an accurate and democratic description of both the ground and first-excited PES [1], its extension to excited-state quantum dynamics requires the knowledge of energy gradients and nonadiabatic couplings. In this work, we show how these properties can be analytically estimated on a quantum computer within the SA-OO-VQE framework, following the coupled-perturbed equations [19–25]. In analogy with Ref. 1, the performance of our algorithm is illustrated on the minimal Schiff base model (*i.e.* the formalimine molecule), for which results are indistinguishable from its classical analog, the (coupled-perturbed) SA-CASSCF method.

The paper is organized as follows. For pedagogical purposes, we briefly introduce quantum chemistry for excited-state in Sec. II A, from the Born–Openheimer approximation in Sec. II A 1 to the SA-MCSCF method in Sec. II A 2. Turning to quantum computing in Sec. II B, a summary of the SA-OO-VQE in given in Sec. II B 1, and a way to extract the eigenstates (*i.e.* the adiabatic states) is provided in Sec. II B 2, where we also discuss the alternative choice of having diabatic or adiabatic states within the SA-OO-VQE algorithm. The analytical estimation of energy gradients and nonadiabatic couplings is then described in Secs. II B 3 and II B 4, respectively, and they are compared with classical methods in Sec. IV B. Using the equations for the analytical gradients, a geometry optimization to the degeneracy point is performed in Sec. IV C as a simple illustration. Conclusions and perspectives are finally discussed in Sec. V.

II. THEORY

A. Quantum Chemistry for excited states

1. Born–Oppenheimer and the adiabatic approximation

One of the most fundamental approximations used in theoretical chemistry is the adiabatic approximation between electrons and nuclei, which most often takes the form of the Born–Oppenheimer approximation and sometimes of the Born–Huang approximation (the latter being essentially used for highly-accurate treatments of vibrations in small molecules). In both cases, nonadiabatic couplings due to the action of the kinetic energy operator of the nuclei on the parametric dependence of the adiabatic electronic wavefunctions are neglected; however, the Born–Huang approximation considers nuclear-mass-dependent diagonal corrections that are to be added to the potential energy surface obtained as a single adiabatic eigenvalue of the clamped-nucleus Hamiltonian.

Such approximations are justified by the small ratio of electronic over nuclear masses, which results in very different energy and time scales in the vast majority of cases. However, electronic degeneracies may occur at certain nuclear geometries (Jahn–Teller crossings due to symmetry, or, more generally, conical intersections). At such points, the two intersecting potential energy surfaces take locally the shape of a double cone (over a subspace of dimension 2 for a two-state crossing). The two nuclear displacements that lift degeneracy to first order are usually called branching-space vectors; their directions can be identified to the energy gradient difference and first-order nonadiabatic coupling (NAC) vector. Formally, the x -component of the NAC vector between two electronic states $|\Psi_I\rangle$ and $|\Psi_J\rangle$ is defined by

$$D_{IJ} = \left\langle \Psi_I \left| \frac{\partial}{\partial x} \Psi_J \right. \right\rangle. \quad (1)$$

where x represents a given nuclear coordinate and the wavefunctions depend parametrically on it (integration, however, is performed over the electronic Hilbert space only). If the wavefunctions considered in Eq. (1) are exact, they yield

$$D_{IJ} = \frac{1}{E_J - E_I} \langle \Psi_I | \frac{\partial \hat{H}}{\partial x} | \Psi_J \rangle, \quad (2)$$

in virtue of the off-diagonal Hellmann–Feynman theorem. The magnitude of the NAC vector is ill-defined at a conical intersection, since it diverges as the inverse of the energy difference [see Eq. (2)]. The numerator, however, is well-defined and often called the derivative coupling vector; note that the nomenclature is not fixed in the literature. It can be viewed as a transition gradient. The other vector that forms the branching space together with the derivative coupling is the gradient (half) difference,

$$G_{IJ} = \frac{1}{2} \left(\langle \Psi_J | \frac{\partial \hat{H}}{\partial x} | \Psi_J \rangle - \langle \Psi_I | \frac{\partial \hat{H}}{\partial x} | \Psi_I \rangle \right). \quad (3)$$

The vectors G_{IJ} and $(E_J - E_I)D_{IJ}$ – often denoted g and h vectors or x_1 and x_2 vectors in this context – play symmetrical roles: they form the two directions that make the adiabatic energy difference increase to first order from zero at a conical intersection. They actually are undetermined up to within a mutual rotation, which directly reflects the freedom in defining two specific degenerate eigenstates (see, e.g., Ref. [26]).

In addition to being essential for the correct capture of the conical topography of crossings, nonadiabatic couplings are required for describing the coupled equations that govern the nuclear components of the molecular wavefunction. As already pointed out, they become large when the energy gap between electronic states decreases, which is why conical intersections are key for describing radiationless processes whereby population is transferred among electronic states. In practice, nonadiabatic quantum dynamics is often better described in terms of quasidiabatic electronic states that result from a unitary transformation of a relevant subset of coupled adiabatic states. They vary smoothly enough with respect to nuclear coordinates to allow for neglect of kinetic couplings but introduce instead nonzero potential couplings.

Further on this is beyond the scope of the present work and the literature on the subject is vast. We refer for example to Ref. 27 for a comprehensive review of relevant concepts. Finally, let us stress that the ability of a computational method to describe correctly the topography of a conical intersection is intimately related to the formal possibility of using analytic derivative techniques for evaluating nonadiabatic couplings [16]. This somewhat relies on the fact that the final step of the whole computational procedure should be viewed as a Hamiltonian submatrix diagonalization that provides several eigenstates democratically within the same subspace. The state-averaged multi-configurational self-consistent-field (SA-MCSCF) method is an evident option in this context, with analytic derivatives applied similarly to diagonal and off-diagonal terms [21].

2. State-averaged multi-configurational self-consistent-field method (SA-MCSCF)

The electronic structure Hamiltonian reads, in second quantization,

$$\hat{\mathcal{H}} = \sum_{pq} h_{pq} \hat{E}_{pq} + \frac{1}{2} \sum_{pqrs} g_{pqrs} \hat{e}_{pqrs}, \quad (4)$$

where the one- and two-electron integrals are defined as (in real algebra)

$$h_{pq} = \int d\mathbf{r} \phi_p(\mathbf{r}) \left(-\frac{1}{2} \nabla_{\mathbf{r}}^2 + v_{ne}(\mathbf{r}) \right) \phi_q(\mathbf{r}), \quad (5)$$

and

$$g_{pqrs} = \iint d\mathbf{r}_1 d\mathbf{r}_2 \frac{\phi_p(\mathbf{r}_1) \phi_r(\mathbf{r}_2) \phi_q(\mathbf{r}_1) \phi_s(\mathbf{r}_2)}{|\mathbf{r}_1 - \mathbf{r}_2|}, \quad (6)$$

respectively, where $\{\phi_p\}$ are the molecular orbitals defining the (finite) basis set and $v_{ne}(\mathbf{r})$ is the nucleus-electron potential. The one- and two-body spin-free excitation operators are defined such as $\hat{E}_{pq} = \sum_{\sigma} \hat{a}_{p\sigma}^{\dagger} \hat{a}_{q\sigma}$ and $\hat{e}_{pqrs} = \sum_{\sigma, \tau} \hat{a}_{p\sigma}^{\dagger} \hat{a}_{r\tau}^{\dagger} \hat{a}_{s\tau} \hat{a}_{q\sigma}$ where $\hat{a}_{p\sigma}^{\dagger}$ ($\hat{a}_{p\sigma}$) is the creation (annihilation) operator of an electron with spin σ in spatial orbital p . Due to the exponential increase of the configuration space in the number of molecular orbitals, it is of common use to select only a restricted (and, ideally, relevant) part of it in practical calculation, for instance by considering the active space approximation where the orbital space is separated into a set of frozen occupied, active and virtual orbitals. In such a reduced configuration space, the configuration interaction method is not invariant anymore under orbital rotations [11, 28] and the choice of orbitals will influence the quality of the result. Hence, one has to consider the re-optimization of the orbitals, thus leading to the MCSCF model which wavefunction reads:

$$|\Psi(\boldsymbol{\kappa}, \mathbf{c})\rangle = e^{-\hat{\kappa}} \left(\sum_i c_i |\Phi_i\rangle \right), \quad (7)$$

where $\{|\Phi_i\rangle\}$ are Slater determinants or configuration state functions, and $\hat{U}_O(\boldsymbol{\kappa}) = e^{-\hat{\kappa}}$ is the orbital-rotation operator. The latter is defined as follows in the spin-restricted formalism with real algebra:

$$\hat{\kappa} = \sum_{p>q}^{\text{MOs}} \kappa_{pq} (\hat{E}_{pq} - \hat{E}_{qp}). \quad (8)$$

The parameters of the wavefunction in Eq. (7) are determined by variationally optimizing the expectation value of the energy:

$$E = \min_{\boldsymbol{\kappa}, \mathbf{c}} \frac{\langle \Psi(\boldsymbol{\kappa}, \mathbf{c}) | \hat{\mathcal{H}} | \Psi(\boldsymbol{\kappa}, \mathbf{c}) \rangle}{\langle \Psi(\boldsymbol{\kappa}, \mathbf{c}) | \Psi(\boldsymbol{\kappa}, \mathbf{c}) \rangle}. \quad (9)$$

In order to have a democratic description of ground and excited states, one can simultaneously optimize several MCSCF states that are generated from the same orbital basis. As extensively discussed in Ref. 11, it is convenient to introduce an exponential unitary parametrization of the configuration space with nonredundant variables,

$$\hat{U}_C(\mathbf{S}) = e^{-\hat{S}}, \quad (10)$$

where

$$\hat{S} = \sum_J \sum_{K>J} S_{KJ} \left(|\Psi_K^{(0)}\rangle \langle \Psi_J^{(0)}| - |\Psi_J^{(0)}\rangle \langle \Psi_K^{(0)}| \right) \quad (11)$$

and

$$|\Psi_I^{(0)}\rangle = \sum_i c_{Ii}^{(0)} |\Phi_i\rangle \quad (12)$$

are initial orthonormal states built from the same set of molecular orbitals. Within the SA-MCSCF model,

the wavefunctions are subject to a double-exponential parametrization

$$|\Psi_I(\boldsymbol{\kappa}, \mathbf{S})\rangle = e^{-\hat{\kappa}} e^{-\hat{S}} |\Psi_I^{(0)}\rangle, \quad (13)$$

where, according to the generalization of the Rayleigh–Ritz variational principle for an ensemble of ground and excited states [29], the parameters are variationally optimized by minimizing the state-averaged energy

$$E^{\text{SA-MCSCF}} = \min_{\boldsymbol{\kappa}, \mathbf{S}} \sum_I w_I \langle \Psi_I(\boldsymbol{\kappa}, \mathbf{S}) | \hat{\mathcal{H}} | \Psi_I(\boldsymbol{\kappa}, \mathbf{S}) \rangle \quad (14)$$

where $\sum_I w_I = 1$ and the states are automatically orthonormalized as they are generated from unitary transformations of the initial orthonormal states $\{|\Psi_I^{(0)}\rangle\}$. Note that due to the orbital optimization, the converged individual and state-averaged energies may vary with the weights. In practice, the equal weight SA-MCSCF (where all weights are equal) is usually considered. Finally, the dependence on $\boldsymbol{\kappa}$ in the wavefunctions can actually be transferred to the electronic integrals in the Hamiltonian, *i.e.* $h_{pq} \rightarrow h_{pq}(\boldsymbol{\kappa})$ and $g_{pqrs} \rightarrow g_{pqrs}(\boldsymbol{\kappa})$, such that Eq. (14) equivalently reads

$$E^{\text{SA-MCSCF}} = \min_{\boldsymbol{\kappa}, \mathbf{S}} \sum_I w_I \langle \Psi_I(\mathbf{S}) | \hat{\mathcal{H}}(\boldsymbol{\kappa}) | \Psi_I(\mathbf{S}) \rangle, \quad (15)$$

where $\hat{\mathcal{H}}(\boldsymbol{\kappa}) = \hat{U}_O^\dagger(\boldsymbol{\kappa}) \hat{\mathcal{H}} \hat{U}_O(\boldsymbol{\kappa})$ is the MO-basis transformed Hamiltonian.

While the SA-MCSCF method allows for a democratic description of ground and excited states, it is only variational with respect to the state-averaged energy, so that an individual state is not variational. This makes the calculation of analytical energy gradients of each individual state more complicated, as it requires the introduction of specific Lagrangians and the solution of so-called coupled-perturbed equations, as further discussed in Sec. II B 3.

B. Estimation of energies, analytical gradients and nonadiabatic coupling on a quantum computer

1. State-averaged orbital-optimized variational-quantum-eigensolver (SA-OO-VQE)

The variational quantum eigensolver (VQE) [17, 18] represents one of the most promising methods to estimate the ground-state energy on near-term quantum computers. As suggested by the name of the algorithm, the VQE relies on the Rayleigh–Ritz variational principle and consists in finding the closest approximation to the ground-state wavefunction thanks to a given *ansatz* (defined by a parametrized unitary operation $\hat{U}(\boldsymbol{\theta})$). Applying this unitary operation to a chosen initial state (usually very easy to prepare, such as the Hartree–Fock (HF) Slater determinant $|\text{HF}\rangle$) leads to a parametrized trial

wavefunction $|\Psi(\boldsymbol{\theta})\rangle = \hat{U}(\boldsymbol{\theta})|\text{HF}\rangle$, from which the associated energy is estimated by repeated measurements of the quantum circuit. Following the variational principle, one can optimize the parameters $\boldsymbol{\theta}$ on a classical computer until this energy (that is naturally lower bounded) is minimized,

$$E(\boldsymbol{\theta}) = \langle \Psi(\boldsymbol{\theta}) | \hat{\mathcal{H}} | \Psi(\boldsymbol{\theta}) \rangle \geq E_0, \quad (16)$$

where the trial state is normalized by default as we use a unitary transformation $1 = \langle \Psi(\boldsymbol{\theta}) | \Psi(\boldsymbol{\theta}) \rangle = \langle \text{HF} | \text{HF} \rangle$. Unfortunately, the extension of the VQE algorithm to excited state is not trivial, as a variational estimation of the excited-state energies can only be defined under orthogonal constraints. Such constraints have been considered by adding penalization terms to the Hamiltonian, thus leading to the state-specific variational quantum deflation (VQD) algorithm [30–33] where each state is determined by a separate minimization (or only two minimizations in total if the first one is performed on a state-average ensemble [34]). Other extensions can treat excited states on the same footing, but still favor the ground state [35–38]. However, the proper description of conical intersections or avoided crossings require a democratic description of both the ground and excited states. Such an equal footing treatment can be achieved by performing a single minimization (or resolution) for all states sharing the same ansatz, as in multistate-contracted VQE (MC-VQE) [39, 40], fully-weighted subspace-search VQE (SS-VQE) [41], variance-VQE [42] and the quantum filter diagonalization method [43, 44]. Inspired by the SS-VQE method of Nakanishi *et al.* [41], we proposed the (equi-weighted) state-averaged orbital-optimized VQE (SA-OO-VQE), that can be seen as a combination of a state-averaged VQE (SA-VQE) and a state-averaged orbital-optimization (SA-OO) procedure. We are going to present now an summary of this algorithm. For clarity, let us focus on an equi-ensemble of two states (the extension to more electronic states is straightforward).

In the SA-OO-VQE algorithm, we first start with a set of two orthonormal initial states $|\Phi_A\rangle$ and $|\Phi_B\rangle$ (with $\langle \Phi_A | \Phi_B \rangle = 0$) and transform the latter into two trial states with a circuit ansatz (implementing a unitary transformation $\hat{U}(\boldsymbol{\theta})$) such that

$$|\Psi_A(\boldsymbol{\theta})\rangle = \hat{U}(\boldsymbol{\theta})|\Phi_A\rangle \text{ and } |\Psi_B(\boldsymbol{\theta})\rangle = \hat{U}(\boldsymbol{\theta})|\Phi_B\rangle. \quad (17)$$

Both trial states are used to approximate the two low-lying states of the MO-basis dependent Hamiltonian $\hat{\mathcal{H}}(\boldsymbol{\kappa})$. The state-averaged orbital-optimized energy is then defined as (following the Rayleigh–Ritz variational principle for ensembles [29])

$$\begin{aligned} E^{\text{SA-OO-VQE}} &= \min_{\boldsymbol{\kappa}, \boldsymbol{\theta}} \left\{ w_A \langle \Psi_A(\boldsymbol{\theta}) | \hat{\mathcal{H}}(\boldsymbol{\kappa}) | \Psi_A(\boldsymbol{\theta}) \rangle \right. \\ &\quad \left. + w_B \langle \Psi_B(\boldsymbol{\theta}) | \hat{\mathcal{H}}(\boldsymbol{\kappa}) | \Psi_B(\boldsymbol{\theta}) \rangle \right\} \quad (18) \\ &\geq w_A \langle \Psi_0 | \hat{\mathcal{H}}(\boldsymbol{\kappa}^*) | \Psi_0 \rangle + w_B \langle \Psi_1 | \hat{\mathcal{H}}(\boldsymbol{\kappa}^*) | \Psi_1 \rangle \end{aligned}$$

where $E^{\text{SA-OO-VQE}} \equiv E^{\text{SA-OO-VQE}}(\boldsymbol{\kappa}^*, \boldsymbol{\theta}^*)$, $\boldsymbol{\kappa}^*$ and $\boldsymbol{\theta}^*$ denote the minimizing sets of parameters, and w_A and

w_B are the weights attributed to each state with the normalization condition $w_A + w_B = 1$. According to Eq. (18) and the variational principle [29], the SA-OO-VQE energy is lower-bounded by the ensemble energy of the exact two lowest eigenstates (denoted by $|\Psi_0\rangle$ and $|\Psi_1\rangle$) of $\hat{\mathcal{H}}(\kappa^*)$ in the active-space approximation. In practice, the global minimization in Eq. (18) is carried out by alternating minimizations over the MOs κ (while keeping the circuit parameters θ frozen), and θ (while keeping κ frozen), separately, until reaching a global convergence of the SA-OO-VQE energy (see our previous work [1] for more details). We will refer to the above minimizations as the SA-VQE and SA-OO optimizations, respectively. Thus, the main steps of the SA-OO-VQE algorithm can be summarized as follows,

1. **Initialization:** Initialize the circuits with two orthonormal states $|\Phi_A\rangle$ and $|\Phi_B\rangle$.

2. **SA-VQE:** Apply a quantum ansatz (*i.e.* a given quantum circuit) to transform both initial states into trial states $|\Psi_A(\theta)\rangle = \hat{U}(\theta)|\Phi_A\rangle$ and $|\Psi_B(\theta)\rangle = \hat{U}(\theta)|\Phi_B\rangle$, and find the optimal set of circuit parameters that minimizes the state-averaged energy

$$\theta^* = \arg \min_{\theta} E^{\text{SA-OO-VQE}}(\kappa, \theta) \quad (19)$$

for a fixed orbital basis κ .

3. **SA-OO:** Rotate the orbital basis to find the optimal set of parameters that minimize the state-averaged energy

$$\kappa^* = \arg \min_{\kappa} E^{\text{SA-OO-VQE}}(\kappa, \theta) \quad (20)$$

(*e.g.* with Newton-Raphson), for a fixed set of parameters θ .

4. **SA-OO-VQE:** Repeat steps 2 and 3 until the state-average energy is minimized with respect to both θ and κ , *i.e.* find

$$(\kappa^*, \theta^*) = \arg \min_{\kappa, \theta} E^{\text{SA-OO-VQE}}(\kappa, \theta). \quad (21)$$

As discussed in previous works [1, 41], the lower bound in Eq. (18) is uniquely defined if $w_A > w_B$, but is invariant under any rotation between $|\Psi_0\rangle$ and $|\Psi_1\rangle$ in the equi-ensemble case ($w_A = w_B$). Hence, considering the case $w_A = w_B$ does not guarantee that the optimized states $|\Psi_A(\theta^*)\rangle$ and $|\Psi_B(\theta^*)\rangle$ are the closest approximation of the eigenstates $|\Psi_0\rangle$ and $|\Psi_1\rangle$. However, this enforces the definition of a well-defined two-state subspace spanned by either Ψ_A and Ψ_B or Ψ_0 and Ψ_1 , such that

the latter are eigenstates. Forcing this correspondence (that we refer to as the *state-resolution*) is a complicated task that can be handled in different ways. Considering $w_A > w_B$ is a straightforward solution, but this constraint may complicate the SA-VQE optimization considerably [41]. Additional tricks can be used in the equi-ensemble case, by considering additional cost-functions to be maximized [41], a classical diagonalization [39], or another type of cost-functions that use the variance of the states [42]. In Sec. II B 2, we discuss another approach, inspired by the one of Nakanishi [41], to solve the state-resolution of a two-state ensemble within the SA-OO-VQE algorithm, when the initial states are the HF Slater determinant and any singlet singly-excited configuration interaction (CIS) state. Note that while we focus on those particular initial states in this manuscript, any other choice could in principle be considered.

2. State-resolution procedure

As discussed in the previous section, the state-resolution (*i.e.* the capture of the active-space eigenvectors of $\hat{\mathcal{H}}(\kappa)$) at each call of the SA-VQE sub-algorithm may in practice involve different manipulations that either significantly increase the number of measures [39], or necessitate more complex cost functions that can be harder to minimize [41, 42]. We propose another method that requires few additional gates and a negligible increase in the number of measurements.

Our approach takes advantage of the rotational invariance of the equi-ensemble state-averaged energy and postpone the state-resolution to the very end of the SA-OO-VQE algorithm. Considering the equi-ensemble (*i.e.* $w_A = w_B$), after convergence of the SA-OO-VQE algorithm, the resulting Hilbert space spanned by $|\Psi_A(\theta^*)\rangle$ and $|\Psi_B(\theta^*)\rangle$ is a good approximation to the subspace spanned the SA-CASSCF states – classical analog of SA-OO-VQE method –, within the same active space. (As discussed in Sec. II B 1, the SA-OO-VQE states are not constrained to be the eigenvectors of $\hat{\mathcal{H}}$, or, equivalently, to form the adiabatic basis that diagonalizes $\hat{\mathcal{H}}(\kappa^*)$). To resolve the ground and first excited SA-OO-VQE *eigenstates* (which should be good approximations to $|\Psi_0^{\text{SA-CASSCF}}\rangle$ and $|\Psi_1^{\text{SA-CASSCF}}\rangle$), we propose to implement a rotation between the initial states $|\Phi_A\rangle$ and $|\Phi_B\rangle$, such that the new rotated initial states become

$$\begin{aligned} |\Phi_0(\varphi)\rangle &= \cos \varphi |\Phi_A\rangle + \sin \varphi |\Phi_B\rangle, \\ |\Phi_1(\varphi)\rangle &= -\sin \varphi |\Phi_A\rangle + \cos \varphi |\Phi_B\rangle, \end{aligned} \quad (22)$$

where we have the property $|\Phi_1(\varphi)\rangle = |\Phi_0(\varphi + \pi/2)\rangle$. After applying the ansatz with optimized parameters θ^* , these new rotated initial states evolve to

$$\begin{aligned} |\Psi_0(\varphi, \theta^*)\rangle &= \cos \varphi |\Psi_A(\theta^*)\rangle + \sin \varphi |\Psi_B(\theta^*)\rangle, \\ |\Psi_1(\varphi, \theta^*)\rangle &= -\sin \varphi |\Psi_A(\theta^*)\rangle + \cos \varphi |\Psi_B(\theta^*)\rangle, \end{aligned} \quad (23)$$

which leads to a rotation between the final SA-OO-VQE states. Note that they remain orthonormal and, by virtue

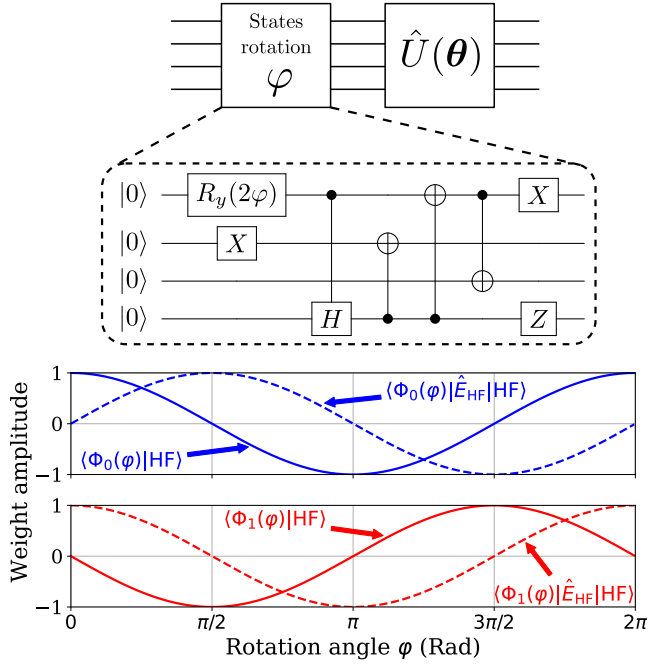


Figure 1. **Upper panel:** Short-depth quantum circuit specifically designed for the state-resolution of the SA-OO-VQE algorithm, to build the state $|\Phi(\varphi)\rangle = \cos \varphi |\Phi_A\rangle + \sin \varphi |\Phi_B\rangle$, i.e. a rotation between the HF state $|\Phi_A\rangle = |\text{HF}\rangle$ and the HOMO-LUMO singlet CIS state $|\Phi_B\rangle = \hat{E}_{\text{hl}}|\text{HF}\rangle/\sqrt{2}$. **Lower panel:** Overlaps $\langle\Phi_{0/1}(\varphi)|\text{HF}\rangle$ and $\langle\Phi_{0/1}(\varphi)|\hat{E}_{\text{hl}}|\text{HF}\rangle$ as a function of the rotation parameter φ .

of the equi-ensembles properties, lead to the same state-averaged energy that is invariant with respect to φ . The state-resolution amounts to finding the value $\varphi \rightarrow \varphi^*$ that minimizes the energy of $|\Psi_0(\varphi, \theta^*)\rangle$,

$$\varphi^* = \arg \min_{\varphi} \langle \Psi_0(\theta^*, \varphi) | \hat{H}(\kappa^*) | \Psi_0(\theta^*, \varphi) \rangle \quad (24)$$

(or, equivalently, maximizes the one of $|\Psi_1(\varphi, \theta^*)\rangle$), thus making both $|\Psi_0(\varphi^*, \theta^*)\rangle$ and $|\Psi_1(\varphi^*, \theta^*)\rangle$ approximated eigenstates of $\hat{H}(\kappa^*)$. Satisfying Eq. (24) can be seen as the fifth step of the SA-OO-VQE algorithm (see Sec. II B 1 for the first four steps). In Fig. 1, we show the short-depth circuit we specifically developed to perform the rotation between the HF determinant $|\Phi_A\rangle = |\text{HF}\rangle$ and a singlet-excited CIS state $|\Phi_B\rangle = \hat{E}_{\text{hl}}|\text{HF}\rangle/\sqrt{2}$, where ‘h’ and ‘l’ refer to the HOMO and LUMO orbitals, respectively. In practice, the circuit works as follows (for the sake of simplicity, we focus on a 2-orbitals – i.e. 4-qubits – and 2-electron CAS). Starting with the 4 qubits in the $|0\rangle$ state, a $R_y(2\varphi)$ rotation gate and a X gate are applied to the first and second qubit, respectively, thus leading to the quantum superposition

$$R_y^0(2\varphi)X^1|0000\rangle = \cos \varphi |0100\rangle + \sin \varphi |1100\rangle. \quad (25)$$

Then, a controlled-Hadamard gate transforms the state $|1100\rangle$ into $\frac{1}{\sqrt{2}}(|1100\rangle + |1101\rangle)$, which evolves into

$\frac{1}{\sqrt{2}}(|1110\rangle + |0001\rangle)$ after applying three CNOT gates. The first term in the right hand side of Eq. (25) remains invariant with respect to the aforementioned operations, such that the state now reads

$$\cos \varphi |0100\rangle + \frac{\sin \varphi}{\sqrt{2}}(|1110\rangle + |0001\rangle). \quad (26)$$

Finally, we apply X and Z gates to the first and last qubits, respectively, to arrive at the final expression

$$\begin{aligned} |\Phi_0(\varphi)\rangle &= \cos \varphi |1100\rangle + \frac{\sin \varphi}{\sqrt{2}}(|0110\rangle - |1001\rangle) \\ &= \cos \varphi |\Phi_A\rangle + \sin \varphi |\Phi_B\rangle, \end{aligned} \quad (27)$$

where $|\Phi_A\rangle = |\text{HF}\rangle$ and $|\Phi_B\rangle = \hat{E}_{\text{hl}}|\text{HF}\rangle/\sqrt{2} = (|1001\rangle - |0110\rangle)/\sqrt{2}$ is the HOMO-LUMO singlet-excited CIS state. Replacing $\varphi \rightarrow \varphi + \pi/2$ in Eq. (27), one recovers $|\Phi_1(\varphi)\rangle$ in Eq. (22), such that the parameter φ can be tuned to realize any real linear combination between $|\Phi_A\rangle$ and $|\Phi_B\rangle$, as illustrated in the lower panels of Fig. 1. Note that this circuit is valid for any singlet-excited CIS state $|\Phi_B\rangle$, by simply applying the quantum gates to the qubits associated to the orbitals involved in the excitation.

Note that the idea introduced here for the state-resolution procedure in SA-OO-VQE follows closely the one proposed by Nakanishi *et al.* (Sec II.A. of Ref. 41). Indeed, the additional circuit in Fig. 1 is equivalent to their additional unitary operation $V(\phi)$, for which we provide an explicit form for any two-state ensemble (with a specific focus on initial states that are the HF and any singlet-excited CIS states). Note also that a SA-OO and SA-VQE algorithms are alternatively employed in our method. The resulting SA-OO-VQE subspace is then more meaningful in terms of electronic correlations as it (ideally) provides analog results as in the SA-CASSCF method, contrary to the SS-VQE scheme that is equivalent to the CASCI method. Because we work with an equi-ensemble, the state-resolution can be performed at the very end of the SA-OO-VQE algorithm only. This attractive feature of the equi-ensemble SA-OO-VQE allows in principle to spare a lot of unnecessary quantum resources, as one can still end up with the (approximate) eigenstates without requiring harder optimization procedures or additional quantum measurements at each instance of the SA-VQE algorithm.

3. Analytical gradients

In this section, we turn towards the question of the analytical evaluation of individual-state nuclear energy gradient with the SA-OO-VQE algorithm (which will be noted $|\Psi_I\rangle$, with $I = 0, 1, \dots$). As opposed to the state-specific orbital-optimized VQE introduced by Mizukami *et al.* [45], each set of variational parameters (in our case θ and κ) is not optimized to minimize each individual-

state energy,

$$\frac{\partial E_I(\boldsymbol{\kappa}, \boldsymbol{\theta})}{\partial \kappa_{pq}} \neq 0, \frac{\partial E_I(\boldsymbol{\kappa}, \boldsymbol{\theta})}{\partial \theta_n} \neq 0, \quad (28)$$

but rather to minimize the state-averaged energy,

$$\frac{\partial E_{SA}(\boldsymbol{\kappa}, \boldsymbol{\theta})}{\partial \kappa_{pq}} = \frac{\partial E_{SA}(\boldsymbol{\kappa}, \boldsymbol{\theta})}{\partial \theta_n} = 0, \quad (29)$$

which renders the estimation of the individual-state nuclear energy gradients more complicated, as it has to take into account the non-variational character of the method. Fortunately, one can build analytical Lagrangians that are fully variational with respect to every parameter [46], such that their optimization facilitate the estimation of the targeted quantities (*e.g.* energy derivatives and nonadiabatic couplings in our case).

Following this strategy, we build an individual-state Lagrangian \mathcal{L}_I that depends on all the parameters as follows,

$$\mathcal{L}_I = E_I + \left(\sum_{pq} \bar{\kappa}_{pq}^I \frac{\partial E_{SA}}{\partial \kappa_{pq}} - 0 \right) + \left(\sum_n \bar{\theta}_n^I \frac{\partial E_{SA}}{\partial \theta_n} - 0 \right). \quad (30)$$

Note that, based on the state-averaged variational conditions given in Eq. (29), the correspondence $\mathcal{L}_I = E_I$ holds here. In the definition of the Lagrangian \mathcal{L}_I , the parameters $\bar{\kappa}_{pq}^I$ and $\bar{\theta}_n^I$ are Lagrange multipliers designed to make it fully stationary such that

$$\frac{\partial \mathcal{L}_I}{\partial \bar{\kappa}_{pq}^I} = \frac{\partial \mathcal{L}_I}{\partial \bar{\theta}_n^I} = \frac{\partial \mathcal{L}_I}{\partial \kappa_{pq}} = \frac{\partial \mathcal{L}_I}{\partial \theta_n} = 0. \quad (31)$$

To fulfil the stationary conditions in Eq. (31), the Lagrange multipliers are determined by solving the so-called coupled-perturbed equations

$$\begin{aligned} \frac{\partial \mathcal{L}_I}{\partial \kappa_{rs}} &= \frac{\partial E_I}{\partial \kappa_{rs}} + \sum_{pq} \bar{\kappa}_{pq}^I H_{pq,rs}^{OO} + \sum_n \bar{\theta}_n^I H_{n,rs}^{CO} = 0, \\ \frac{\partial \mathcal{L}_I}{\partial \theta_m} &= \frac{\partial E_I}{\partial \theta_m} + \sum_{pq} \bar{\kappa}_{pq}^I H_{pq,m}^{OC} + \sum_n \bar{\theta}_n^I H_{n,m}^{CC} = 0, \end{aligned} \quad (32)$$

where we have introduced

$$H_{pq,rs}^{OO} = \frac{\partial^2 E_{SA}}{\partial \kappa_{pq} \partial \kappa_{rs}}, \quad (33)$$

$$H_{n,m}^{CC} = \frac{\partial^2 E_{SA}}{\partial \theta_n \partial \theta_m}, \quad (34)$$

$$H_{n,rs}^{CO} = \frac{\partial^2 E_{SA}}{\partial \theta_n \partial \kappa_{rs}}, \quad (35)$$

which correspond to matrix elements of the (state-averaged) orbital hessian \mathbf{H}^{OO} , circuit hessian \mathbf{H}^{CC} and circuit-orbital hessian \mathbf{H}^{CO} (with $\mathbf{H}^{CO} = (\mathbf{H}^{OC})^T$). The remaining terms

$$G_{rs}^{O,I} = \frac{\partial E_I}{\partial \kappa_{rs}} \quad \text{and} \quad G_m^{C,I} = \frac{\partial E_I}{\partial \theta_m}, \quad (36)$$

are elements of the circuit gradient vector $\mathbf{G}^{C,I}$ and the orbital gradient vector $\mathbf{G}^{O,I}$ of the state $|\Psi_I(\boldsymbol{\theta})\rangle$. The orbital gradient for individual states $G_{pq}^{O,I}$ can be relatively easily computed from their one- and two-RDMs and MO coefficients. The state-averaged orbital Hessian $H_{pq,rs}^{OO}$ can also be determined from the state-averaged one- and two-RDMs and MO coefficients [20, 24]. Therefore, they do not require any additional measurements on the quantum computer. However, the first and second derivatives of the state-averaged energy with respect to the circuit parameters requires many more measurements according to the parameter-shift rule [47] (or any other practical way to measure it out of a circuit). For the sake of conciseness, we refer the interested reader to Appendix A for more details about the estimation of the above Hessian matrices and gradients vectors.

Assuming we have evaluated the necessary Hessian matrices and gradient vectors out of a quantum circuit following Appendix A, the Lagrange multipliers $\bar{\kappa}_{pq}^I$ and $\bar{\theta}_n^I$ satisfying the conditions in Eq. (31) are determined on a classical computer by solving the following matrix equation

$$\begin{pmatrix} \mathbf{H}^{OO} & \mathbf{H}^{OC} \\ \mathbf{H}^{CO} & \mathbf{H}^{CC} \end{pmatrix} \begin{pmatrix} \bar{\boldsymbol{\kappa}}^I \\ \bar{\boldsymbol{\theta}}^I \end{pmatrix} = - \begin{pmatrix} \mathbf{G}^{O,I} \\ \mathbf{G}^{C,I} \end{pmatrix}. \quad (37)$$

Inserting these Lagrange multipliers back into Eq. (30) makes the Lagrangian fully stationary, and the property $\frac{dE_I}{dx} = \frac{d\mathcal{L}_I}{dx} = \frac{\partial \mathcal{L}_I}{\partial x}$ holds [46]. Hence, the energy derivative $\frac{dE_I}{dx}$ can be evaluated as follows:

$$\begin{aligned} \frac{dE_I}{dx} &= \sum_{pq} \frac{\partial h_{pq}}{\partial x} \gamma_{pq}^{I,\text{eff}} + \frac{1}{2} \sum_{pqrs} \frac{\partial g_{pqrs}}{\partial x} \Gamma_{pqrs}^{I,\text{eff}} \\ &\quad + \sum_J \sum_n \omega_J \bar{\theta}_n^I G_n^{C,J} \left(\frac{\partial \hat{H}}{\partial x} \right), \end{aligned} \quad (38)$$

with effective 1- and 2-RDMs defined by

$$\boldsymbol{\gamma}^{I,\text{eff}} = \boldsymbol{\gamma}^I + \tilde{\boldsymbol{\gamma}}^{I,SA} \quad (39)$$

$$\boldsymbol{\Gamma}^{I,\text{eff}} = \boldsymbol{\Gamma}^I + \tilde{\boldsymbol{\Gamma}}^{I,SA} \quad (40)$$

with $\gamma_{pq}^I = \langle \Psi_I | \hat{E}_{pq} | \Psi_I \rangle$ and $\Gamma_{pqrs}^I = \langle \Psi_I | \hat{e}_{pqrs} | \Psi_I \rangle$ regular RDMs of the reference state $|\Psi_I\rangle$, supplemented by corrective state-averaged RDMs $\tilde{\boldsymbol{\gamma}}^{I,SA}$ and $\tilde{\boldsymbol{\Gamma}}^{I,SA}$ (encoding orbital contributions) with matrix elements

$$\tilde{\gamma}_{pq}^{I,SA} = \sum_o (\gamma_{oq}^{SA} \bar{\kappa}_{op}^I + \gamma_{po}^{SA} \bar{\kappa}_{oq}^I) \quad (41)$$

$$\begin{aligned} \tilde{\Gamma}_{pqrs}^{I,SA} &= \sum_o (\Gamma_{oqrs}^{SA} \bar{\kappa}_{op}^I + \Gamma_{pors}^{SA} \bar{\kappa}_{oq}^I \\ &\quad + \Gamma_{pqos}^{SA} \bar{\kappa}_{or}^I + \Gamma_{pqro}^{SA} \bar{\kappa}_{os}^I). \end{aligned} \quad (42)$$

Note that building these effective matrices does not require any additional measures from the quantum circuit as the RDMs $\boldsymbol{\gamma}^I$ and $\boldsymbol{\Gamma}^I$ are already evaluated during the SA-OO-VQE to estimate the state-averaged energy.

The circuit gradient $G_n^{C,J}(\frac{\partial \hat{\mathcal{H}}}{\partial x})$ introduced in Eq. (38) is defined such that

$$G_n^{C,J}(\frac{\partial \hat{\mathcal{H}}}{\partial x}) = \frac{\partial}{\partial \theta_n} \langle \Psi_J | \frac{\partial \hat{\mathcal{H}}}{\partial x} | \Psi_J \rangle \quad (43)$$

and can be estimated out of a quantum circuit in the same way as for a generic energy gradient using for example the parameter shift-rule (cf Appendix A). The change being here that the central operator is now the nuclear derivative of the Hamiltonian $\partial \hat{\mathcal{H}}/\partial x$ which can be evaluated on a classical computer as shown in Appendix D. Note that, we also refer the interested reader to Appendix D for practical details about nuclear derivatives of electronic integrals (in Eq. (38)) which can be evaluated on a classical computer with common quantum chemistry packages.

Interestingly, compared to its classical analog SA-CASSCF, note that a unique set of circuit parameters θ is considered to simultaneously find both ground and first excited states in SA-OO-VQE, instead of the configuration-interaction (CI) coefficients for each state (denoted by \mathbf{c}_0 and \mathbf{c}_1). This results in a much reduced size of the parameter space,

$$\dim(\theta) \ll \dim(\mathbf{c}_0) + \dim(\mathbf{c}_1). \quad (44)$$

This has important consequences, as the original CP-MCSCF equations sometimes cannot be solved due to memory issues in storing all the matrix elements of \mathbf{H}^{CC} , although some alternative implementations have been proposed to overcome this problem (see Ref. 24 and references therein). Hence, the classical complexity in solving the coupled-perturbed equations [Eq. (37)] is considerably reduced in SA-OO-VQE compared to SA-CASSCF, at the expense of a lower accuracy (as the SA-VQE solver is not exact in contrast to SA-CASSCF).

4. nonadiabatic couplings

We provide now an analytical approach to estimate nonadiabatic couplings from the SA-OO-VQE algorithm. The definition and Hellmann–Feynman formula for the NAC, D_{IJ} , have been given above – see Eq. (1) and Eq. (2) – in the ideal case of exact adiabatic eigenstates. It is well-known in the practical context of an MCSCF ansatz that this term actually splits into two contributions: (i) a typically larger CI-contribution, which obey a Hellmann–Feynman like formula (except that eigenstates are now CI-coefficient vectors and the Hamiltonian operator is replaced by its finite matrix representation in the CSF basis set); (ii) a typically smaller CSF-contribution, which accounts for molecular orbital gradients (via both their expansion coefficients and the overlaps among the primitive atomic basis functions); see, e.g., Ref. [21]. However, in SA-OO-VQE we work with non-variational external parameters which makes the NAC more complex to evaluate from a practical point of view. Fortunately, coupled-perturbed equations have been derived to

take into account the non-variational character of wavefunctions which are based on the same machinery as for gradient calculation [19–25]. To proceed, one solves the following set of coupled linear equations

$$\begin{pmatrix} \mathbf{H}^{\text{OO}} & \mathbf{H}^{\text{OC}} \\ \mathbf{H}^{\text{CO}} & \mathbf{H}^{\text{CC}} \end{pmatrix} \begin{pmatrix} \bar{\kappa}^{IJ} \\ \bar{\mathbf{c}}^{IJ} \end{pmatrix} = - \begin{pmatrix} \mathbf{G}^{\text{O},IJ} \\ 0 \end{pmatrix}, \quad (45)$$

to determine the NAC Lagrange multipliers $(\bar{\kappa}^{IJ}, \bar{\mathbf{c}}^{IJ})$. Here, we retrieve the same Hessian block as for the gradient calculation and $G_{pq}^{\text{O},IJ} = \langle \Psi_I | (\partial \mathcal{H} / \partial \kappa_{pq}) | \Psi_J \rangle$ represents the interstate orbital coupling gradient whose elements can be easily measured out of a quantum computer (using for example methods provided in Ref. [41]). Once the multipliers are determined using a classical computer, the NAC can be evaluated such that

$$\begin{aligned} D_{IJ} = \frac{1}{E_J - E_I} & \left(\sum_{pq} \frac{\partial h_{pq}}{\partial x} \gamma_{pq}^{IJ, \text{eff}} + \frac{1}{2} \sum_{pqrs} \frac{\partial g_{pqrs}}{\partial x} \Gamma_{pqrs}^{IJ, \text{eff}} \right. \\ & \left. + \sum_K \sum_n \omega_K \bar{\mathbf{c}}_n^{IJ} G_n^{C,K}(\frac{\partial \hat{\mathcal{H}}}{\partial x}) \right) \\ & - \frac{1}{2} \sum_{pq} \gamma_{pq}^{IJ} ((\partial_x p|q) - (q|\partial_x p)). \end{aligned} \quad (46)$$

The effective transition 1- and 2-RDMs introduced here are defined by

$$\gamma^{IJ, \text{eff}} = \gamma^{IJ} + \tilde{\gamma}^{IJ, \text{SA}} \quad (47)$$

$$\Gamma^{IJ, \text{eff}} = \Gamma^{IJ} + \tilde{\Gamma}^{IJ, \text{SA}} \quad (48)$$

and $\tilde{\gamma}^{IJ, \text{SA}}$ and $\tilde{\Gamma}^{IJ, \text{SA}}$ are the orbital contributions to the 1- and 2-RDMs, respectively. These state-averaged matrices are defined in a same way as in Eq. 41 (we replace $\bar{\kappa}^I$ by $\bar{\kappa}^{IJ}$ in this case). In Eq. 46, the terms in parenthesis encode the off-diagonal Hellman–Feynman contribution complemented by additional corrective terms accounting for the non-variational character of the wavefunctions due to orbital and quantum circuit optimization. The contribution outside parenthesis is the so-called “CSF-term” which formally takes into account the variation of the Slater-determinants due to nuclear displacement (see Ref. [19] for more details). The elements $(\partial_x p|q)$ represent half-derivative of MOs’ overlap which can be easily estimated with most quantum chemistry packages. Note the presence of transition 1 and 2-RDMs in Eq. 46 defined such as $\gamma_{pq}^{IJ} = \langle \Psi_I | \hat{E}_{pq} | \Psi_J \rangle$ and $\Gamma_{pqrs}^{IJ} = \langle \Psi_I | \hat{e}_{pqrs} | \Psi_J \rangle$. These matrices can be obtained from a quantum circuit using methods to determine transition matrix elements such as the one provided in Ref. [41].

III. COMPUTATIONAL DETAILS

To test our theoretical developments, we consider the formaldehyde molecule CH_2NH : a minimal Schiff base

model, relevant for the study of the photoisomerization in larger bio-molecules (such as the RPSB molecule whose *cis* to *trans* isomerization plays a key role in the visual cycle process [48–50]). An illustration of the geometry of the molecule is shown in Fig. 2a.

In analogy with our previous study [1], we freeze and constrain the N-CH₂ part of the molecule in the same plane. The interatomic distances are $d_{\text{N-C}} = 1.498$ Å, $d_{\text{C-H}} = 1.067$ Å, $d_{\text{N-H}} = 0.987$ Å and the angle $\widehat{\text{N-C-H}} = 118.36^\circ$. The second H atom is symmetric to the first one with respect to the N-C axis. The two remaining degrees of freedom characterize the out-of-plane bending angle $\alpha \equiv \widehat{\text{H-N-C}}$ and the dihedral angle $\phi \equiv \widehat{\text{H-N-C-H}}$. For practical calculations, the cc-pVDZ basis is used and an active space of two electrons in two orbitals (2,2) is considered. The orbital optimization is realized over the 43 spatial-orbitals of the system (for SA-OO-VQE and SA-CASSCF). Reference quantum chemistry calculations are realized with OpenMolcas [51] whereas the Psi4 [52] package is used to provide SA-OO-VQE with initial data about the molecular system.

The simulation of the SA-OO-VQE algorithm is realized using the python quantum computing packages OpenFermion [53] and Cirq [54]. The ansatz we employ in the SA-VQE algorithm is a generalized unitary coupled cluster ansatz with spin-free double-excitation operators (GUCCD) such that

$$\hat{U}(\boldsymbol{\theta}) = e^{\hat{T}(\boldsymbol{\theta}) - \hat{T}^\dagger(\boldsymbol{\theta})}, \quad (49)$$

$$\hat{T}(\boldsymbol{\theta}) = \sum_{t,v,w,u}^{\text{active}} \theta_{tuvw} \sum_{\sigma,\tau=\uparrow,\downarrow} \hat{a}_{t\sigma}^\dagger \hat{a}_{v\tau}^\dagger \hat{a}_{w\tau} \hat{a}_{u\sigma}. \quad (50)$$

We refer the interested reader to our previous work [1] for more details about the GUCCD ansatz. Our simulation considers circuit parameters $\boldsymbol{\theta}$ initialized to zero and optimized using the “Sequential Least Squares Programming” (SLSQP) method from the python Scipy package. For each call of SA-VQE, the SLSQP method is run with a maximum number of 500 iterations and a precision threshold of 10^{-8} Ha. The threshold for the global convergence of SA-OO-VQE is also set to 10^{-8} Ha. A home-made python code has been developed to implement the state-averaged Netwon-Raphson algorithm required for the SA-OO subalgorithm.

IV. NUMERICAL RESULTS

A. Illustration of the final state resolution in SA-OO-VQE

As discussed in Sec. II B 2, the SA-OO-VQE states obtained after optimizing the $\boldsymbol{\kappa}$ and $\boldsymbol{\theta}$ parameters do not correspond to the eigenstates of $\hat{H}(\boldsymbol{\kappa})$, and an additional rotation between the initial states is required (also called state-resolution). In Fig. 2, we illustrate

the convergence of each step of the SA-OO-VQE algorithm applied to the formalimine molecule, depicted in panel (a), with geometry parameters set to $\phi = 80^\circ$ and $\alpha = 100^\circ$. The ground, first-excited and state-averaged energies are plotted on panel (b) for each step of the SA-OO-VQE algorithm, where SA-VQE and SA-OO phases are represented by white and grey strips, respectively. The ground and first-excited SA-CASSCF reference energies are also provided for comparison, as well as the state-averaged SA-CASSCF energy which forms a natural lower bound for SA-OO-VQE [see Eq. (18)]. As readily seen in panel (b), alternating between the SA-VQE and the SA-OO algorithms progressively lowers the state-averaged energy, requiring three full SA-OO-VQE cycles to reach global convergence. At convergence, this energy has an error of only $\sim 10^{-6}$ Ha with respect to SA-CASSCF, indicating that the subspace spanned by the SA-OO-VQE trials states is a very good approximation to the one spanned by the SA-CASSCF states. However, the converged individual SA-OO-VQE states differ significantly from the SA-CASSCF states (at the end of the third SA-OO-VQE step in panel (b)). Hence, one has to apply to state-resolution described in Sec. II B 2 to recover the correct eigenstates. This final step is symbolized by the blue region in panel (b), where we employ the rotation circuit shown in Fig. 1 and optimize the rotation parameter φ such that the energies are effectively pushed as far as possible from each other, thus maximizing the difference between the first-excited and ground-state energies. After this final step, the individual SA-OO-VQE energies are in very good agreement with the SA-CASSCF ones (with an error of $\sim 10^{-6}$ Ha, similar to the state-averaged energy error).

In panels (c) and (d) of Fig. 2, we show the one-dimensional (1D) PES along the α -angle, obtained from SA-OO-VQE and SA-CASSCF for a dihedral angle $\phi = 80^\circ$. More precisely, we compare the 1D-PES of SA-OO-VQE without (panel (c)) and with (panel (d)) the final state-resolution procedure. As readily seen in these two panels, the state-averaged SA-OO-VQE energy is in a very good agreement with the reference state-averaged SA-CASSCF energy all over the 1D-PES (with an error $< 10^{-6}$ Ha). Without state-resolution (see panel (c)), the individual-state energies are globally different from the SA-CASSCF ones, especially for $\alpha < 150^\circ$. For $\alpha > 150^\circ$, the energies of the individual states match the reference ones, showing that the state-resolution is not always necessary to capture the eigenstates. Interestingly, the SA-OO-VQE states smoothly cross around $\alpha \sim 132^\circ$. As discussed in Ref. 1, this results from the use of an equi-ensemble where no ordering of the trial states is enforced. In such a case, the converged SA-OO-VQE states will naturally evolve to the state that is the closest to its initial state, *i.e.* with the highest overlap with its initial state (see Ref. 1 for more details). Typically, when $\alpha < 132^\circ$ the singlet single-excited CIS state $|\Phi_B\rangle = \hat{E}_{\text{hl}}|\text{HF}\rangle$ has the largest contribution to the SA-CASSCF ground state, while for $\alpha > 132^\circ$ the

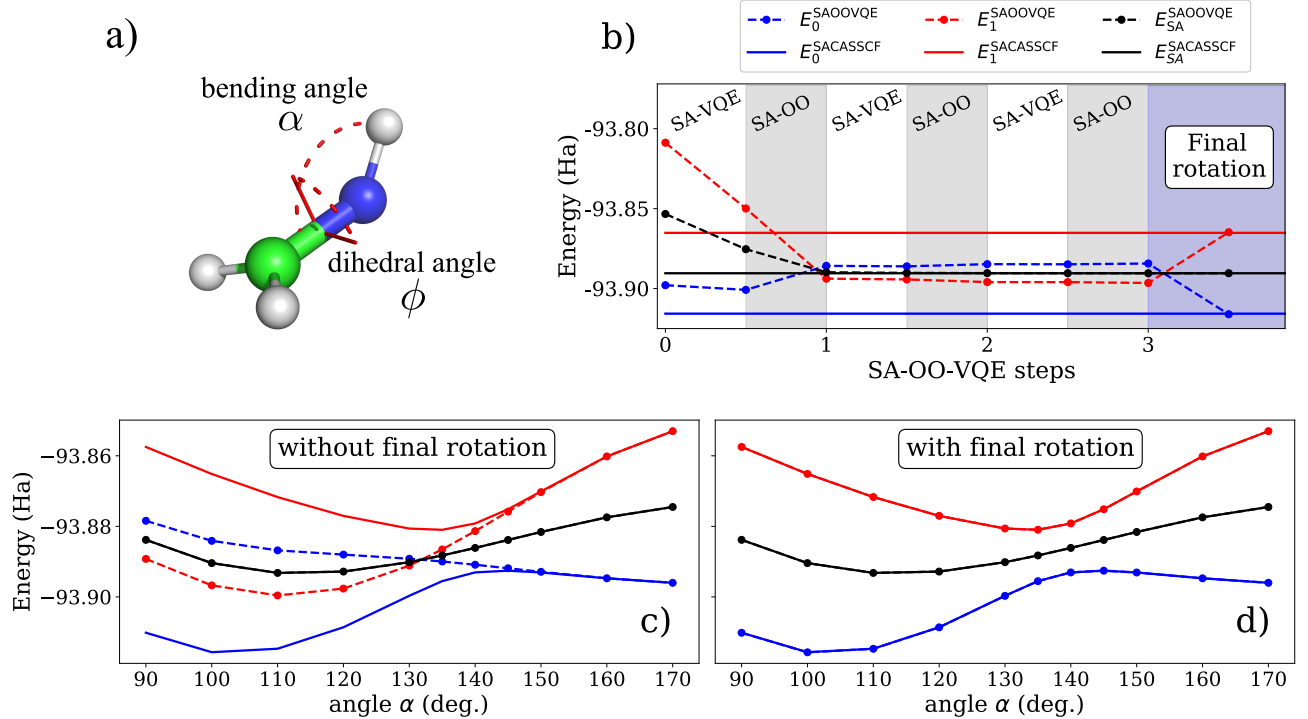


Figure 2. **Illustration of the convergence of each step of the equi-ensemble SA-OO-VQE algorithm.** In all panels, dashed and solid lines represent the SA-OO-VQE and SA-CASSCF energies, respectively. **a)** Geometry of the formalimine molecule with the bending angle $\alpha = \widehat{\text{NCH}}$ and the dihedral angle $\phi = \widehat{\text{HCNH}}$. **b)** Evolution of the state-averaged energy during the different steps of the SA-OO-VQE algorithm for $\phi = 80^\circ$ and $\alpha = 100^\circ$. White and grey strips represent SA-VQE and SA-OO phases, respectively, while the blue strip represents the final state-resolution step. Converged SA-OO-VQE 1D-PES scans along α with $\phi = 80^\circ$ are shown before **(c)** and after **(d)** the state-resolution procedure.

$|\Phi_A\rangle = |\text{HF}\rangle$ has the largest contribution (and reciprocally for the first-excited SA-CASSCF state). The state-resolution procedure (see panel (d)) will lift the crossing, thus resulting in an avoided-crossing captured by the adiabatic eigenstates and an excellent agreement between the SA-OO-VQE and SA-CASSCF energies.

B. Calculation of analytical gradients and nonadiabatic couplings

Let us now turn to the nuclear gradients and nonadiabatic couplings of the adiabatic states obtained after convergence of the SA-OO-VQE algorithm (with state-resolution), following Eqs. (38) and (46). They are represented in Figs. 4 and 3 along the α direction for $\phi = 80^\circ$ and $\phi = 90^\circ$, respectively. As readily seen in Figs. 4 and 3, both the analytical gradients and the NAC calculated from our SA-OO-VQE implementation and SA-CASSCF are indistinguishable, with a negligible difference of the order of 10^{-3} mHa/degree for the gradients and 10^{-3} degree $^{-1}$ for the NAC amplitudes (all over the PES). This supports the derivations of Eqs. (38) and (46) and shows that SA-OO-VQE can provide (ideally, *i.e.* without noise) as accurate results as its classical analog.

Turning to the energy landscape of Fig. 4 (panel (a)) with $\phi = 80^\circ$ (exactly the same as Fig. 2, panel (d), but plotted again here for convenience), we observe an avoided crossing between the ground and first-excited states around $\alpha = 140^\circ$. This particular behavior can also be detected by looking at the amplitudes of the NAC (panel (c) of Fig. 4), which increase significantly at the avoided crossing position (but without diverging).

In contrast, the 1D-PES shows a crossing (a conical intersection here) for $\phi = 90^\circ$ (see panel (a) of Fig. 3). This very different behaviour is manifested by a discontinuity in the gradients $\partial E_0/\partial\alpha$ and $\partial E_1/\partial\alpha$ that suddenly inverse their position at the crossing point $\alpha \approx 137^\circ$, while the gradients are smoothly evolving along the 1D-PES when the states do not cross (see panel (b) of Figs. 4 and 3, respectively). This is the direct consequence of the presence of a degeneracy in the energy profile. In contrast to the α direction (panel (b)), the fact that the gradients $\partial E_0/\partial\phi$ and $\partial E_1/\partial\phi$ are zero for all α (see panel (d) in Fig. 3) reveals the presence of extrema for both states in the ϕ direction. This behaviour is consistent with $\phi = 90^\circ$ defining a higher-symmetry domain (C_{2v} point group), wherein there is no interstate coupling (different irreducible representations) and local extrema are induced for both potential energies at $\phi = 90^\circ$. For

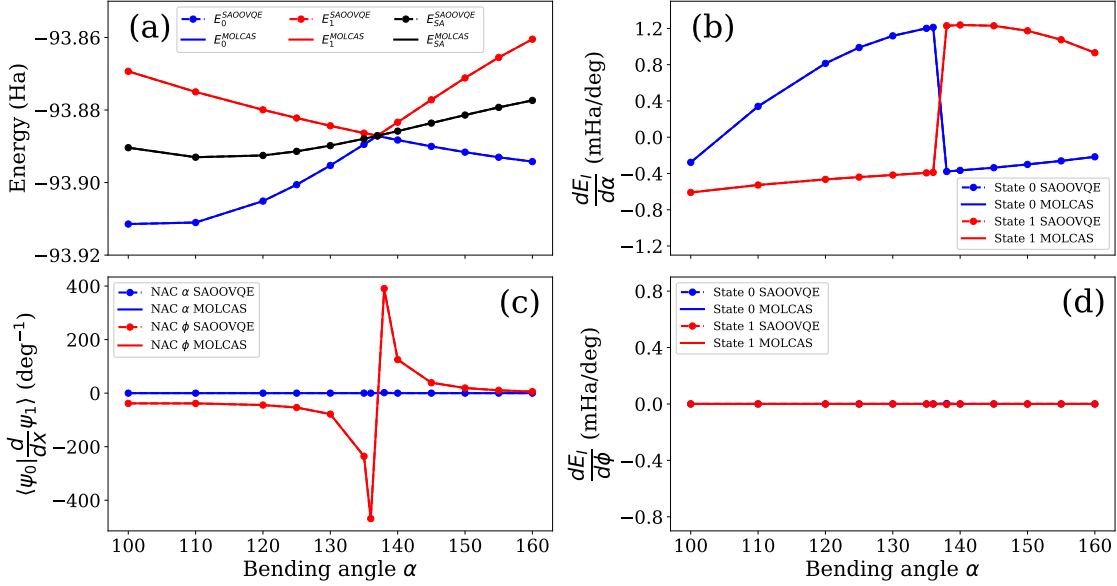


Figure 3. **Energy gradients and NAC with respect to the bending angle α with $\phi = 90^\circ$.** SA-OO-VQE results are shown in dashed lines with dots while solid lines are for the reference SA-CASSCF results. The ground and first-excited state energies are represented by blue and red colors, respectively. (a) Potential energy surfaces (b) Analytical individual-state energy gradients [Eq. (38) for $x = \alpha$] (c) nonadiabatic coupling vector $\langle \Psi_0 | (\partial/\partial x) \Psi_1 \rangle$ for $x = \alpha$ (blue) and $x = \phi$ (red) (d) Analytical individual-state energy gradients [Eq. (38) for $x = \phi$].

a better illustration, these local extrema along the ϕ direction are shown in Fig. 5 and correspond to the intersection points between the grey plane (defining $\phi = 90^\circ$) and the two-dimensional (α, ϕ) -PESs computed with SA-OO-VQE.

Considering now the nonadiabatic couplings (panel (c) of Fig. 3), we find that it points to a direction perpendicular to the gradients. This is expected, as the NAC together with the gradient of the energy difference span the branching space defined by α and ϕ , as discussed in Sec. II A 1. The NAC exhibits an asymptotic discontinuity around the conical intersection, caused by the term $(E_1 - E_0)^{-1}$ which goes to infinity at this degeneracy point. The increase of the NAC amplitude at the avoided crossing or its divergence at the conical intersection is the expected manifestation of its linear dependence on the inverse of the energy difference (see Eq. (2)). This typically results in a break-down of the Born–Oppenheimer approximation, which is consistent with observing radiationless population transfer from the first-excited state back to the ground state. This will essentially occur around such crossing geometries along the photochemical reaction path. A prototypical example is the photoisomerization process in the retinal chromophore of rhodopsin [7]. In such a situation, quantum dynamics simulations (or their various flavours of quantum-classical approximations) must explicitly account for NAC-terms within the equations of motion for the nuclei evolving within a manifold of coupled electronic states.

C. Geometry optimization to locate formaldimine’s conical intersection in the (α, ϕ) space

As an application to the SA-OO-VQE analytical gradients, we perform a geometry optimization inside the (α, ϕ) -plane to find a conical intersection for formaldimine. To do so, we use a steepest-descent optimization algorithm considering as a cost function the energy difference $\Delta E = E_1^{\text{SAOOVQE}} - E_0^{\text{SAOOVQE}}$. At each step of the run, we update the molecular geometry in the (α, ϕ) -plane based on the associated gradient

$$\mathbf{g}_{\Delta E} = \frac{dE_1^{\text{SAOOVQE}}}{d\mathbf{x}} - \frac{dE_0^{\text{SAOOVQE}}}{d\mathbf{x}} \quad (51)$$

which is evaluated using our analytical method described in Sec. II B (with $\mathbf{x} = (\alpha, \phi)$).

An example run of the algorithm is shown in Fig. 6, where the steepest-descent procedure starts at point (a) for a molecular configuration $(\alpha, \phi) = (130^\circ, 35^\circ)$. The path followed during the geometry optimization is driven by the vector $-\mathbf{g}_{\Delta E}$ which is illustrated at every 6 iterations with arrows in left panel of Fig. 6 (out of a total of 48 iterations required to reach the conical intersection point). Similarly, in the right panel of the figure the vector $-\mathbf{g}_{\Delta E}$ is represented with red arrows (starting from the Hydrogen atom) for four molecular geometries (a), (b), (c) and (d) obtained on the path of optimization (also noted in left panel). From Fig. 6 we see that the path realized stays orthogonal to isolines ($\Delta E = c$ with c constant) of the cost function ΔE . This feature indicates

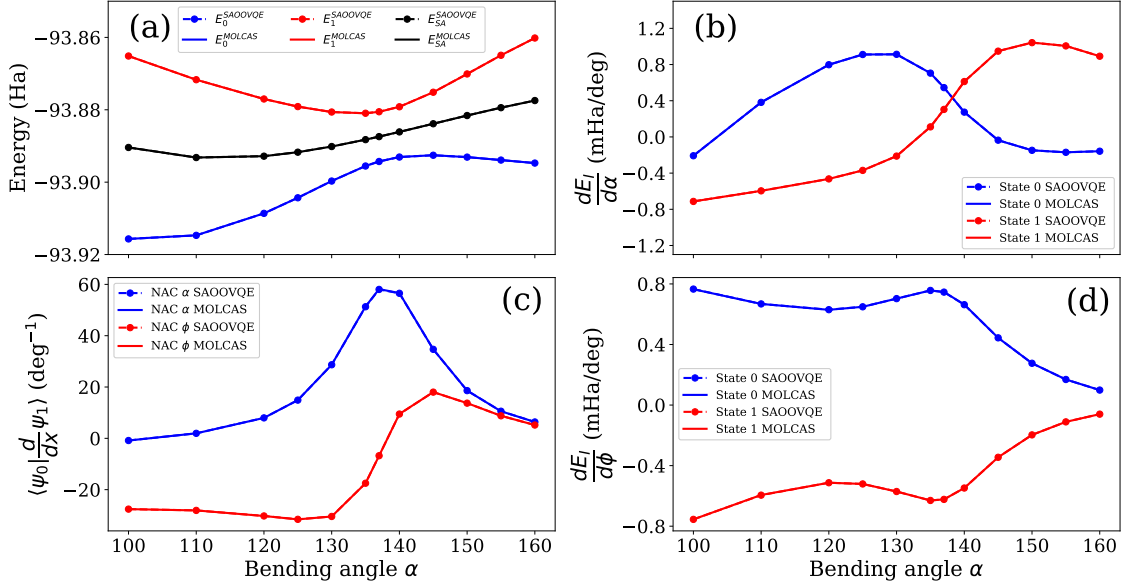


Figure 4. **Energy gradients and NAC with respect to the bending angle α with $\phi = 80^\circ$.** SA-OO-VQE results are shown in dashed lines with dots while solid lines are for the reference SA-CASSCF results. The ground and first-excited state energies are represented by blue and red colors, respectively. (a) Potential energy surfaces (b) Analytical individual-state energy gradients [Eq. (38) for $x = \alpha$] (c) nonadiabatic coupling vector $\langle \Psi_0 | (\partial/\partial x) \Psi_1 \rangle$ for $x = \alpha$ (blue) and $x = \phi$ (red) (d) Analytical individual-state energy gradients [Eq. (38) for $x = \phi$].

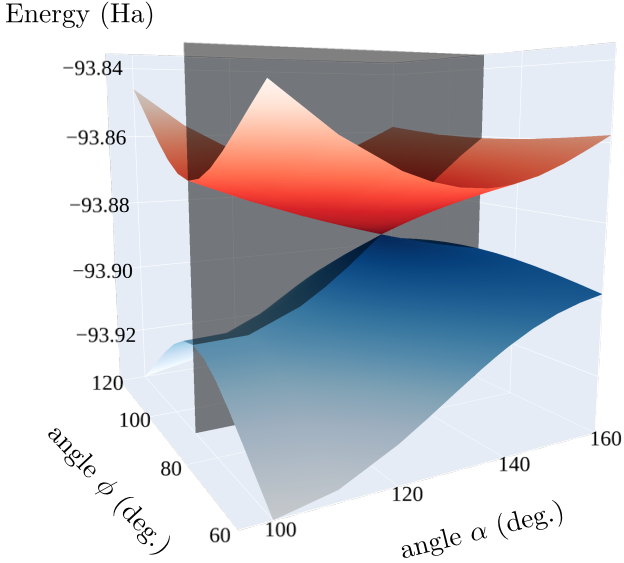


Figure 5. **(α, ϕ) -PES for the formalimine molecule.** The energies are obtained with the SA-OO-VQE algorithm after a full resolution of the states. A conical intersection is observed around the geometry ($\alpha = 136.95^\circ$, $\phi = 90^\circ$). Grey plane is defined for $\phi = 90^\circ$ and intersects both PESs at extrema values in the ϕ direction.

that the SA-OO-VQE algorithm provides consistent pairs of gradients for the two states, thus leading smoothly to the molecular geometry associated to the conical intersection in the (α, ϕ) -plane. At the end of the geometry

optimization, the conical intersection is found for a geometry $\phi = 90^\circ$ and $\alpha = 139.6^\circ$. As a comparison, note that a similar calculation has been realized with the SA-CASSCF method. Our observations in this case were that a similar path was taken in the (α, ϕ) -plane leading then to an equivalent location of the conical intersection with a negligible difference of the final molecular geometry (error $\sim 0.001^\circ$ for both α and ϕ). In practice, note that the non-smooth behavior of the cost function at the conical intersection makes the gradient-descent algorithm hard to converge when approaching this point (as the gradient of the cost function will always have a non-zero component in either direction). As the scope of this paper is to provide proof-of-principle calculation, we simply stopped the algorithm after a limited number of iterations.

As a final remark, note that this paper focuses on the localization of a conical intersection within the (α, ϕ) 2D-subspace at fixed values of the other internal coordinates. As this subspace is a good description of the branching space, there is a unique point of degeneracy (the conical intersection) within this plane where degeneracy is lifted to first order from it. As such, minimising ΔE , and nothing else, is sufficient, as the complement space is frozen. A more general procedure where the other internal coordinates are not frozen would require a general optimization algorithm towards the minimal energy crossing point (MECP), where the information about the nonadiabatic couplings is needed. Examples of MECP-optimization algorithms can be found in Refs. 55–58. The implementation of such algorithms follows on from this manuscript

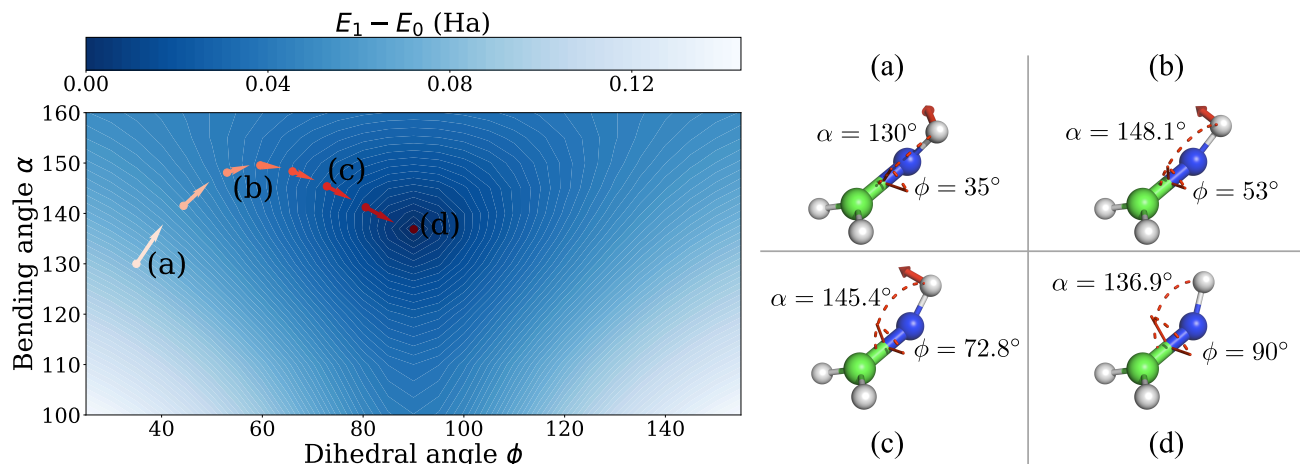


Figure 6. **(α, ϕ)-Geometry optimization to the conical intersection point.** **Left panel:** optimization path of a steepest-descent algorithm to locate the conical intersection of formalimine. The contourplot shows the energy difference $\Delta E = E_1 - E_0$, and the vectors represent the negative of the gradient of the energy difference $\mathbf{g}_{\Delta E}$ at each point of the optimization. **Right panel:** Four molecular geometries corresponding to four points of the optimization, denoted by (a), (b), (c) and (d) on the left panel. The corresponding (α, ϕ) angles and $\mathbf{g}_{\Delta E}$ vectors are shown.

and is left for future work.

V. CONCLUSIONS AND PERSPECTIVES

In this paper, we have introduced several tools to improve our original SA-OO-VQE algorithm [1]. The first improvement consists in introducing a flexible and efficient way to resolve the SA-OO-VQE electronic states. The method, based on equi-ensemble properties, takes advantage of the invariance of the state-averaged energy under rotation of the states involved in the ensemble. Using a simple rotation of the input states (implemented by a short-depth circuit), we show that one can postpone the resolution of the electronic states to the very end of the full SA-OO-VQE scheme, thus avoiding many unnecessary manipulations and quantum measures during intermediate steps of the algorithm. The second aspect investigated is the development of theoretical methods to extract analytical derivatives from the SA-OO-VQE which are fundamental for the study of molecular systems: the nuclear energy gradients and nonadiabatic couplings. The Lagrangian methods we employed are intimately linked to the classical coupled-perturbed theory introduced earlier in quantum chemistry. We numerically demonstrated the good agreement between our estimation of the energy gradient and the nonadiabatic couplings against reference results based on SA-CASSCF calculations. Finally, to illustrate the use of these derivatives in practical calculations, we realized a geometry optimization based on SA-OO-VQE simulation to locate a conical intersection of the formalimine molecule. The results obtained are providing a very accurate localization of the spectral degeneracy compared to predictions given by SA-CASSCF energy landscapes.

The definition of these new tools opens the way to several new developments. One aspect that we already briefly touched upon above, is the definition of the intermediate diabatic and final adiabatic bases. In our implementation of the SA-OO-VQE algorithm, the procedure starts from reference guess states and has no reason to produce “excessive” transformations: this thus makes the potentially least-transformed subspace a good candidate for being a quasidiabatic representation (see Ref. 59). At the moment we have been observing such a property and we have good incentive but no formal proof. Further work is under way to show that SA-OO-VQE before its final diagonalization could be an efficient avenue indeed for the *ab initio* production of relevant quasidiabatic states. Such results would be important as it would facilitate use in molecular quantum dynamics applications. With an appropriate definition of such states and construction of an quantum-classical interface these tools can benefit from classical implementations [60] of algorithms to perform various forms of molecular dynamics [61, 62], thus giving quantum co-processing a firm place in the toolbox of quantum chemical simulations. A related aspect is to consider different kinds of surface couplings, like those provided by the spin-orbit operator. This is of interest for a range of applications, e.g. the rate of intersystem crossing that is key to technological applications as the construction of more efficient blue light emitting diodes. Here we note that it is possible to work with a different set of trial states than the Hartree-Fock and the singlet excited model wave functions chosen in the current work. The latter can be replaced by a triplet excited wave function, while the former can also be a non-ground state determinant (or other simple wave function) if we are interested in excited state couplings.

VI. NOTE ADDED

As we were finalizing the writing process of this manuscript, a similar work appeared on the arXiv [63]. While they show how to estimate analytical gradients in several excited-state extensions of VQE (which we only do for SA-OO-VQE), our work adds several features to

theirs, such as the analytical estimation of nonadiabatic couplings and a discussion on the capture of diabatic versus nonadiabatic states within SA-OO-VQE. This paper and Ref. 63 are therefore complementary, and they both pave the way towards excited-state quantum dynamics with excited-state VQE extensions.

-
- [1] S. Yalouz, B. Senjean, J. Günther, F. Buda, T. E. O'Brien, and L. Visscher, A state-averaged orbital-optimized hybrid quantum-classical algorithm for a democratic description of ground and excited states, *Quantum Sci. Technol.* **6**, 024004 (2021).
 - [2] P. Verma and D. G. Truhlar, Status and challenges of density functional theory, *Trends in Chemistry* **2**, 302 (2020).
 - [3] C. Adamo and D. Jacquemin, The calculations of excited-state properties with time-dependent density functional theory, *Chemical Society Reviews* **42**, 845 (2013).
 - [4] Z. Wang, C. Wu, and W. Liu, Nac-tdfft: Time-dependent density functional theory for nonadiabatic couplings, *Accounts of Chemical Research* **54**, 3288 (2021), pMID: 34448566, <https://doi.org/10.1021/acs.accounts.1c00312>.
 - [5] C. A. Rozzi, F. Troiani, and I. Tavernelli, Quantum modeling of ultrafast photoinduced charge separation, *Journal of Physics: Condensed Matter* **30**, 013002 (2017).
 - [6] N. Minezawa and T. Nakajima, Trajectory surface hopping molecular dynamics simulation by spin-flip time-dependent density functional theory, *The Journal of chemical physics* **150**, 204120 (2019).
 - [7] S. Gozem, H. L. Luk, I. Schapiro, and M. Olivucci, Theory and simulation of the ultrafast double-bond isomerization of biological chromophores, *Chemical reviews* **117**, 13502 (2017).
 - [8] F. Agostini, S. K. Min, A. Abedi, and E. Gross, Quantum-classical nonadiabatic dynamics: Coupled-vs independent-trajectory methods, *Journal of chemical theory and computation* **12**, 2127 (2016).
 - [9] S. Faraji, S. Matsika, and A. I. Krylov, Calculations of non-adiabatic couplings within equation-of-motion coupled-cluster framework: Theory, implementation, and validation against multi-reference methods, *The Journal of chemical physics* **148**, 044103 (2018).
 - [10] S. Lee, Y. Horbatenko, M. Filatov, and C. H. Choi, Fast and accurate computation of nonadiabatic coupling matrix elements using the truncated leibniz formula and mixed-reference spin-flip time-dependent density functional theory, *The Journal of Physical Chemistry Letters* **12**, 4722 (2021).
 - [11] T. Helgaker, P. Jorgensen, and J. Olsen, *Molecular electronic-structure theory* (John Wiley & Sons, 2014).
 - [12] T. Shiozaki, W. Györfly, P. Celani, and H.-J. Werner, Communication: Extended multi-state complete active space second-order perturbation theory: Energy and nuclear gradients, *J. Chem. Phys.* **135**, 081106 (2011).
 - [13] A. A. Granovsky, Extended multi-configuration quasidegenerate perturbation theory: The new approach to multi-state multi-reference perturbation theory, *J. Chem. Phys.* **134**, 214113 (2011).
 - [14] J. W. Park, Analytical gradient theory for quasidegenerate n-electron valence state perturbation theory (qdvpt2), *Journal of chemical theory and computation* **16**, 326 (2019).
 - [15] C. Angeli, S. Borini, M. Cestari, and R. Cimiraglia, A quasidegenerate formulation of the second order n-electron valence state perturbation theory approach, *The Journal of chemical physics* **121**, 4043 (2004).
 - [16] S. Gozem, F. Melaccio, A. Valentini, M. Filatov, M. Huix-Rotllant, N. Ferré, L. M. Frutos, C. Angeli, A. I. Krylov, A. A. Granovsky, *et al.*, Shape of multireference, equation-of-motion coupled-cluster, and density functional theory potential energy surfaces at a conical intersection, *J. Chem. Theory Comput.* **10**, 3074 (2014).
 - [17] A. Peruzzo, J. McClean, P. Shadbolt, M.-H. Yung, X.-Q. Zhou, P. J. Love, A. Aspuru-Guzik, and J. L. O'Brien, A variational eigenvalue solver on a photonic quantum processor, *Nature Comm.* **5**, 4213 (2014).
 - [18] J. R. McClean, J. Romero, R. Babbush, and A. Aspuru-Guzik, The theory of variational hybrid quantum-classical algorithms, *New J. Phys.* **18**, 023023 (2016).
 - [19] B. H. Lengsfeld III, P. Saxe, and D. R. Yarkony, On the evaluation of nonadiabatic coupling matrix elements using sa-mcscf/ci wave functions and analytic gradient methods. i, *The Journal of chemical physics* **81**, 4549 (1984).
 - [20] J. Stårling, A. Bernhardsson, and R. Lindh, Analytical gradients of a state average mcscf state and a state average diagnostic, *Mol. Phys.* **99**, 103 (2001).
 - [21] B. H. Lengsfeld and D. R. Yarkony, Nonadiabatic interactions between potential energy surfaces: Theory and applications, *Advances in chemical physics* **82**, 1 (1992).
 - [22] D. Yarkony, *Modern electronic structure theory*, Vol. 2 (World Scientific, 1995).
 - [23] J. W. Snyder Jr, E. G. Hohenstein, N. Luehr, and T. J. Martínez, An atomic orbital-based formulation of analytical gradients and nonadiabatic coupling vector elements for the state-averaged complete active space self-consistent field method on graphical processing units, *The Journal of chemical physics* **143**, 154107 (2015).
 - [24] J. W. Snyder Jr, B. S. Fales, E. G. Hohenstein, B. G. Levine, and T. J. Martínez, A direct-compatible formulation of the coupled perturbed complete active space self-consistent field equations on graphical processing units, *J. Chem. Phys.* **146**, 174113 (2017).
 - [25] I. Fdez. Galván, M. G. Delcey, T. B. Pedersen, F. Aquilante, and R. Lindh, Analytical state-average complete-active-space self-consistent field nonadiabatic coupling vectors: Implementation with density-fitted two-electron integrals and application to conical intersections, *J. Chem. Theory Comput.* **12**, 3636 (2016).

- [26] F. Gatti, B. Lasorne, H.-D. Meyer, and A. Nauts, Vibronic couplings, in *Applications of Quantum Dynamics in Chemistry* (Springer, 2017) pp. 81–109.
- [27] M. Baer, *Beyond Born-Oppenheimer: Conical intersections and Electronic nonadiabatic coupling terms* (Wiley Online Library, 2006).
- [28] P. E. Siegbahn, J. Almlöf, A. Heiberg, and B. O. Roos, The complete active space scf (casscf) method in a newton–raphson formulation with application to the hno molecule, *J. Chem. Phys.* **74**, 2384 (1981).
- [29] E. K. Gross, L. N. Oliveira, and W. Kohn, Rayleigh-ritz variational principle for ensembles of fractionally occupied states, *Phys. Rev. A* **37**, 2805 (1988).
- [30] O. Higgott, D. Wang, and S. Brierley, Variational quantum computation of excited states, *Quantum* **3**, 156 (2019).
- [31] T. Jones, S. Endo, S. McArdle, X. Yuan, and S. C. Benjamin, Variational quantum algorithms for discovering hamiltonian spectra, *Phys. Rev. A* **99**, 062304 (2019).
- [32] P. Jouzdani, S. Bringuier, and M. Kostuk, A method of determining excited-states for quantum computation, [arXiv:1908.05238](https://arxiv.org/abs/1908.05238) (2019).
- [33] Y. Ibe, Y. O. Nakagawa, T. Yamamoto, K. Mitarai, Q. Gao, and T. Kobayashi, Calculating transition amplitudes by variational quantum eigensolvers, [arXiv:2002.11724](https://arxiv.org/abs/2002.11724) (2020).
- [34] J. Wen, D. Lv, M.-H. Yung, and G.-L. Long, Variational quantum packaged deflation for arbitrary excited states, *Quantum Engineering*, e80 (2021).
- [35] J. R. McClean, M. E. Kimchi-Schwartz, J. Carter, and W. A. de Jong, Hybrid quantum-classical hierarchy for mitigation of decoherence and determination of excited states, *Phys. Rev. A* **95**, 042308 (2017).
- [36] J. I. Colless, V. V. Ramasesh, D. Dahlen, M. S. Blok, M. Kimchi-Schwartz, J. McClean, J. Carter, W. De Jong, and I. Siddiqi, Computation of molecular spectra on a quantum processor with an error-resilient algorithm, *Phys. Rev. X* **8**, 011021 (2018).
- [37] P. J. Ollitrault, A. Kandala, C.-F. Chen, P. K. Barkoutsos, A. Mezzacapo, M. Pistoia, S. Sheldon, S. Woerner, J. Gambetta, and I. Tavernelli, Quantum equation of motion for computing molecular excitation energies on a noisy quantum processor, [arXiv:1910.12890](https://arxiv.org/abs/1910.12890) (2019).
- [38] M. Motta, C. Sun, A. T. Tan, M. J. O’Rourke, E. Ye, A. J. Minnich, F. G. Brandão, and G. K.-L. Chan, Determining eigenstates and thermal states on a quantum computer using quantum imaginary time evolution, *Nat. Phys.* **16**, 205 (2020).
- [39] R. M. Parrish, E. G. Hohenstein, P. L. McMahon, and T. J. Martínez, Quantum computation of electronic transitions using a variational quantum eigensolver, *Phys. Rev. Lett.* **122**, 230401 (2019).
- [40] R. M. Parrish, E. G. Hohenstein, P. L. McMahon, and T. J. Martínez, Hybrid quantum/classical derivative theory: Analytical gradients and excited-state dynamics for the multistate contracted variational quantum eigensolver, [arXiv:1906.08728](https://arxiv.org/abs/1906.08728) (2019).
- [41] K. M. Nakanishi, K. Mitarai, and K. Fujii, Subspace-search variational quantum eigensolver for excited states, *Phys. Rev. Res.* **1**, 033062 (2019).
- [42] D.-B. Zhang, Z.-H. Yuan, and T. Yin, Variational quantum eigensolvers by variance minimization, [arXiv:2006.15781](https://arxiv.org/abs/2006.15781) (2020).
- [43] R. M. Parrish and P. L. McMahon, Quantum filter diagonalization: Quantum eigendecomposition without full quantum phase estimation, [arXiv:1909.08925](https://arxiv.org/abs/1909.08925) (2019).
- [44] T. A. Bespalova and O. Kyriienko, Hamiltonian operator approximation for energy measurement and ground state preparation, [arXiv:2009.03351](https://arxiv.org/abs/2009.03351) (2020).
- [45] W. Mizukami, K. Mitarai, Y. O. Nakagawa, T. Yamamoto, T. Yan, and Y.-y. Ohnishi, Orbital optimized unitary coupled cluster theory for quantum computer, [arXiv:1910.11526](https://arxiv.org/abs/1910.11526) (2019).
- [46] T. U. Helgaker and J. Almlöf, A second-quantization approach to the analytical evaluation of response properties for perturbation-dependent basis sets, *International journal of quantum chemistry* **26**, 275 (1984).
- [47] K. Mitarai, M. Negoro, M. Kitagawa, and K. Fujii, Quantum circuit learning, *Phys. Rev. A* **98**, 032309 (2018).
- [48] M. Chahre, Trigger and amplification mechanisms in visual phototransduction, *Annual review of biophysics and biophysical chemistry* **14**, 331 (1985).
- [49] R. R. Birge, Nature of the primary photochemical events in rhodopsin and bacteriorhodopsin, *Biochimica et Biophysica Acta (BBA)-Bioenergetics* **1016**, 293 (1990).
- [50] C. Schnedermann, X. Yang, M. Liebel, K. Spillane, J. Lugtenburg, I. Fernández, A. Valentini, I. Schapiro, M. Olivucci, P. Kukura, *et al.*, Evidence for a vibrational phase-dependent isotope effect on the photochemistry of vision, *Nature chemistry* **10**, 449 (2018).
- [51] I. Fdez. Galván, M. Vacher, A. Alavi, C. Angeli, F. Aquilante, J. Autschbach, J. J. Bao, S. I. Bokarev, N. A. Bogdanov, R. K. Carlson, L. F. Chibotaru, J. Creutzberg, N. Dattani, M. G. Delcey, S. S. Dong, A. Dreuw, L. Freitag, L. M. Frutos, L. Gagliardi, F. Gen-dron, A. Giussani, L. González, G. Grell, M. Guo, C. E. Hoyer, M. Johansson, S. Keller, S. Knecht, G. Kovačević, E. Källman, G. Li Manni, M. Lundberg, Y. Ma, S. Mai, J. P. Malhado, P. Å. Malmqvist, P. Marquetand, S. A. Mewes, J. Norell, M. Olivucci, M. Oppel, Q. M. Phung, K. Pierloot, F. Plasser, M. Reiher, A. M. Sand, I. Schapiro, P. Sharma, C. J. Stein, L. K. Sørensen, D. G. Truhlar, M. Ugandi, L. Ungur, A. Valentini, S. Vancoillie, V. Veryazov, O. Weser, T. A. Wesolowski, P.-O. Widmark, S. Wouters, A. Zech, J. P. Zobel, and R. Lindh, Openmolcas: From source code to insight, *J. Chem. Theory Comput.* **15**, 5925 (2019), pMID: 31509407, <https://doi.org/10.1021/acs.jctc.9b00532>.
- [52] D. G. Smith, L. A. Burns, A. C. Simmonett, R. M. Parrish, M. C. Schieber, R. Galvelis, P. Kraus, H. Kruse, R. Di Remigio, A. Alenaizan, *et al.*, Psi4 1.4: Open-source software for high-throughput quantum chemistry, *The Journal of Chemical Physics* **152**, 184108 (2020).
- [53] J. R. McClean, N. C. Rubin, K. J. Sung, I. D. Kivlichan, X. Bonet-Monroig, Y. Cao, C. Dai, E. S. Fried, C. Gidney, B. Gimby, P. Gokhale, T. Häner, T. Hardikar, V. Havlíček, O. Higgott, C. Huang, J. Isaac, Z. Jiang, X. Liu, S. McArdle, M. Neeley, T. O’Brien, B. O’Gorman, I. Ozfidan, M. D. Radin, J. Romero, N. P. D. Sawaya, B. Senjean, K. Setia, S. Sim, D. S. Steiger, M. Steudtner, Q. Sun, W. Sun, D. Wang, F. Zhang, and R. Babbush, Openfermion: the electronic structure package for quantum computers, *Quantum Sci. Technol.* (2020).
- [54] C. Developers, *Cirq* (2021), See full list of authors on Github: <https://github.com/quantumlib/Cirq/graphs/-contributors>.

- [55] M. R. Manaa and D. R. Yarkony, On the intersection of two potential energy surfaces of the same symmetry. systematic characterization using a lagrange multiplier constrained procedure, *J. Chem. Phys.* **99**, 5251 (1993).
- [56] M. J. Bearpark, M. A. Robb, and H. B. Schlegel, A direct method for the location of the lowest energy point on a potential surface crossing, *Chem. Phys. Lett.* **223**, 269 (1994).
- [57] T. W. Keal, A. Koslowski, and W. Thiel, Comparison of algorithms for conical intersection optimisation using semiempirical methods, *Theor. Chem. Acc.* **118**, 837 (2007).
- [58] F. Sicilia, L. Blancafort, M. J. Bearpark, and M. A. Robb, New algorithms for optimizing and linking conical intersection points, *Journal of Chemical Theory and Computation* **4**, 257 (2008), pMID: 26620657, <https://doi.org/10.1021/ct7002435>.
- [59] L. Cederbaum, J. Schirmer, and H.-D. Meyer, Block diagonalisation of hermitian matrices, *J. Phys. A Math. Theor.* **22**, 2427 (1989).
- [60] M. Richter, P. Marquetand, J. González-Vázquez, I. Sola, and L. González, SHARC: ab initio molecular dynamics with surface hopping in the adiabatic representation including arbitrary couplings, *J. Chem. Theory Comput.* **7**, 1253 (2011).
- [61] J. C. Tully, Molecular dynamics with electronic transitions, *The Journal of Chemical Physics* **93**, 1061 (1998).
- [62] X. Andrade, A. Castro, D. Zueco, and J. L. Alonso, Modified ehrenfest formalism for efficient large-scale ab initio molecular dynamics, *Journal of Chemical Theory and Computation* **5**, 728 (2009).
- [63] K. Arimitsu, Y. O. Nakagawa, S. Koh, W. Mizukami, Q. Gao, and T. Kobayashi, Analytic energy gradient for state-averaged orbital-optimized variational quantum eigensolvers and its application to a photochemical reaction, *arXiv:2107.12705* (2021).
- [64] Y. Li and S. C. Benjamin, Efficient variational quantum simulator incorporating active error minimization, *Phys. Rev. X* **7**, 021050 (2017).
- [65] M. Schuld, V. Bergholm, C. Gogolin, J. Izaac, and N. Killoran, Evaluating analytic gradients on quantum hardware, *Phys. Rev. A* **99**, 032331 (2019).
- [66] A. Mari, T. R. Bromley, and N. Killoran, Estimating the gradient and higher-order derivatives on quantum hardware, *arXiv:2008.06517* (2020).
- [67] J. J. Meyer, Gradients just got more flexible, *Quantum Views* **5**, 50 (2021).
- [68] T. Hubregtsen, F. Wilde, S. Qasim, and J. Eisert, Single-component gradient rules for variational quantum algorithms, *arXiv:2106.01388* (2021).
- [69] J. Romero, R. Babbush, J. R. McClean, C. Hempel, P. J. Love, and A. Aspuru-Guzik, Strategies for quantum computing molecular energies using the unitary coupled cluster ansatz, *Quantum Sci. Technol.* **4**, 014008 (2018).
- [70] J. S. Kottmann, A. Anand, and A. Aspuru-Guzik, A feasible approach for automatically differentiable unitary coupled-cluster on quantum computers, *arXiv:2011.05938* (2020).
- [71] G. E. Crooks, Gradients of parameterized quantum gates using the parameter-shift rule and gate decomposition, *arXiv:1905.13311* (2019).
- [72] L. Banchi and G. E. Crooks, Measuring analytic gradients of general quantum evolution with the stochastic parameter shift rule, *arXiv:2005.10299* (2020).
- [73] D. Wierichs, J. Izaac, C. Wang, and C. Y.-Y. Lin, General parameter-shift rules for quantum gradients, *arXiv:2107.12390* (2021).
- [74] A. F. Izmaylov, R. A. Lang, and T.-C. Yen, Analytic gradients in variational quantum algorithms: Algebraic extensions of the parameter-shift rule to general unitary transformations, *arXiv:2107.08131* (2021).
- [75] T. Helgaker and P. Jørgensen, Analytical calculation of geometrical derivatives in molecular electronic structure theory, *Advances in quantum chemistry* **19**, 183 (1988).
- [76] J. Simons, P. Jørgensen, and T. U. Helgaker, Higher molecular-deformation derivatives of the configuration-interaction energy, *Chemical physics* **86**, 413 (1984).

Appendix A: Circuit gradient \mathbf{G}^C and Hessian \mathbf{H}^{CC}

Let us consider the estimation of the expectation value M of a generic operator $\hat{\mathcal{M}}$ (in our case the electronic structure Hamiltonian $\hat{\mathcal{H}}$) with respect to a state $|\Psi(\boldsymbol{\theta})\rangle = \hat{U}(\boldsymbol{\theta})|\Phi_0\rangle$,

$$M(\boldsymbol{\theta}) = \text{Tr} [\hat{\mathcal{M}}\rho(\boldsymbol{\theta})] = \langle \Psi(\boldsymbol{\theta}) | \hat{\mathcal{M}} | \Psi(\boldsymbol{\theta}) \rangle, \quad (\text{A1})$$

where $\rho(\boldsymbol{\theta}) = |\Psi(\boldsymbol{\theta})\rangle \langle \Psi(\boldsymbol{\theta})|$ is the density matrix operator and $\text{Tr}[\cdot]$ the trace operation. These matrix elements encode the first order (gradient \mathbf{G}^C) and second order (Hessian \mathbf{H}^{CC}) derivatives with respect to the circuit parameters $\boldsymbol{\theta}$ read as follows

$$G_i^C = \frac{\partial M(\boldsymbol{\theta})}{\partial \theta_i} \quad \text{and} \quad H_{ij}^{CC} = \frac{\partial^2 M(\boldsymbol{\theta})}{\partial \theta_i \partial \theta_j}, \quad (\text{A2})$$

and can be evaluated with the parameter-shift rule [47, 64–68].

As a starting point, let us consider the following unitary:

$$U(\boldsymbol{\theta}) = U_1(\theta_1) \times U_2(\theta_2) \\ = (e^{-i\frac{\theta_1}{2}P_1}e^{-i\frac{\theta_1}{2}\tilde{P}_1}) \times (e^{-i\frac{\theta_2}{2}P_2}e^{-i\frac{\theta_2}{2}\tilde{P}_2}) \quad (\text{A3})$$

where $[P_1, \tilde{P}_1] = [P_2, \tilde{P}_2] = 0$ with the tilde notation denoting a different Pauli string with the same associated parameters, as this is usually the case in the fermionic-UCC ansatz. We have $P_j = P_j^\dagger$ and

$$\frac{\partial U_j(\theta_j)}{\partial \theta_j} = -\frac{i}{2}(P_j + \tilde{P}_j)U_j(\theta_j) \quad (\text{A4})$$

and

$$\left(\frac{\partial U_j(\theta_j)}{\partial \theta_j}\right)^\dagger = -\frac{\partial U_j(\theta_j)}{\partial \theta_j}. \quad (\text{A5})$$

We want to estimate the gradient elements

$$G_i^C = \frac{\partial}{\partial \theta_i} \text{Tr} [\hat{\mathcal{M}}\rho(\boldsymbol{\theta})]. \quad (\text{A6})$$

By taking the derivative with respect to θ_2 , we get

$$\begin{aligned}
G_2^C &= \text{Tr} \left[\frac{\partial}{\partial \theta_2} \hat{\mathcal{M}} \rho(\theta) \right] \\
&= \hat{\mathcal{M}} U_1(\theta_1) \left[\frac{\partial U_2(\theta_2)}{\partial \theta_2} \rho U_2^\dagger(\theta_2) \right. \\
&\quad \left. + U_2(\theta_2) \rho \left(\frac{\partial U_2(\theta_2)}{\partial \theta_2} \right)^\dagger \right] U_1^\dagger(\theta_1) \\
&= -\frac{i}{2} \hat{\mathcal{M}} U_1(\theta_1) \left[(P_2 + \tilde{P}_2) U_2(\theta_2) \rho U_2^\dagger(\theta_2) \right. \\
&\quad \left. - U_2(\theta_2) \rho (P_2 + \tilde{P}_2) U_2^\dagger(\theta_2) \right] U_1^\dagger(\theta_1) \\
&= -\frac{i}{2} \hat{\mathcal{M}} U_1(\theta_1) U_2(\theta_2) \left[(P_2 + \tilde{P}_2), \rho \right] U_2^\dagger(\theta_2) U_1^\dagger(\theta_1)
\end{aligned} \tag{A7}$$

where we used the property $[P_i, U_i(\theta_i)] = 0$ and the notation $\rho = |\Phi_0\rangle \langle \Phi_0|$. We then use the property of commutator for an arbitrary operator [see Eq. (2) in Ref. 47, where $U_j(\theta_j) = \exp(-i\theta_j P_j/2)$],

$$[P_j, \rho] = i \left[U_j \left(\frac{\pi}{2} \right) \rho U_j^\dagger \left(\frac{\pi}{2} \right) - U_j \left(-\frac{\pi}{2} \right) \rho U_j^\dagger \left(-\frac{\pi}{2} \right) \right], \tag{A8}$$

which can be easily demonstrated by considering the property of exponential of Pauli strings

$$e^{i\frac{\theta_j}{2} P_j} = \cos \left(\frac{\theta_j}{2} \right) \mathbf{1} - i \sin \left(\frac{\theta_j}{2} \right) P_j. \tag{A9}$$

One then separates $(P_j + \tilde{P}_j)$ as follows:

$$[(P_j + \tilde{P}_j), \rho] = [P_j, \rho] + [\tilde{P}_j, \rho] \tag{A10}$$

such that, by plugging Eq. (A8) into Eq. (A7), the gradient reads

$$\begin{aligned}
G_2^C &= \frac{1}{2} \hat{\mathcal{M}} U_1(\theta_1) \left[e^{-\frac{i}{2}(\theta_2 + \frac{\pi}{2}) P_2} e^{-\frac{i}{2} \theta_2 \tilde{P}_2} \rho e^{\frac{i}{2} \theta_2 \tilde{P}_2} e^{\frac{i}{2}(\theta_2 + \frac{\pi}{2}) P_2} \right. \\
&\quad - e^{-\frac{i}{2}(\theta_2 - \frac{\pi}{2}) P_2} e^{-\frac{i}{2} \theta_2 \tilde{P}_2} \rho e^{\frac{i}{2} \theta_2 \tilde{P}_2} e^{\frac{i}{2}(\theta_2 - \frac{\pi}{2}) P_2} \\
&\quad + e^{-\frac{i}{2} \theta_2 P_2} e^{-\frac{i}{2}(\theta_2 + \frac{\pi}{2}) \tilde{P}_2} \rho e^{\frac{i}{2}(\theta_2 + \frac{\pi}{2}) \tilde{P}_2} e^{\frac{i}{2} \theta_2 P_2} \\
&\quad \left. - e^{-\frac{i}{2} \theta_2 P_2} e^{-\frac{i}{2}(\theta_2 - \frac{\pi}{2}) \tilde{P}_2} \rho e^{\frac{i}{2}(\theta_2 - \frac{\pi}{2}) \tilde{P}_2} e^{\frac{i}{2} \theta_2 P_2} \right] U_1^\dagger(\theta_1)
\end{aligned} \tag{A11}$$

which, by taking the trace of it, leads to the final expression

$$G_2^C = \frac{1}{2} \left(\langle \hat{\mathcal{M}} \rangle_{\theta_2^+} - \langle \hat{\mathcal{M}} \rangle_{\theta_2^-} + \langle \hat{\mathcal{M}} \rangle_{\tilde{\theta}_2^+} - \langle \hat{\mathcal{M}} \rangle_{\tilde{\theta}_2^-} \right) \tag{A12}$$

where the notation $\langle \hat{\mathcal{M}} \rangle_{\theta_j^\pm}$ refers to the expectation value of the operator $\hat{\mathcal{M}}$ when θ_j has been shifted by $\pm\pi/2$ in front of P_j (and in front of \tilde{P}_j for $\langle \hat{\mathcal{M}} \rangle_{\tilde{\theta}_j^\pm}$).

Generalizing Eq. (A12) to any n -fold fermionic excitation generator \mathcal{G}_j associated to the parameter θ_j leads to the parameter-shift rule:

$$G_j^C = \frac{1}{2} \sum_n^{\forall P_n \in \mathcal{G}_j} \left(\langle \hat{\mathcal{M}} \rangle_{\theta_{j_n}^+} - \langle \hat{\mathcal{M}} \rangle_{\theta_{j_n}^-} \right) \tag{A13}$$

where θ_{j_n} refers to the parameter associated to the Pauli string P_n coming from the fermionic generator \mathcal{G}_j . Note that the parameter-shift rule only applies to generators \mathcal{G} that have at most two distinct eigenvalues [65], which is always the case for any Pauli string but not a linear combination of them. However, each parameter θ_j is associated to two Pauli strings for a single-excitation fermionic operator, to eight Pauli strings for a double-excitation fermionic operator, and to 2^{2n-1} Pauli strings for a n -fold fermionic excitation operator [69, 70], such that

$$e^{i\frac{\theta}{2} \mathcal{G}} \rightarrow \prod_{x=1}^{2^{2n-1}} e^{i\frac{\theta}{2} P_x}. \tag{A14}$$

The above formula is actually an equality because Pauli strings resulting from a same n -fold fermionic excitation operator actually commute with each other [69]. Although the fermionic generator \mathcal{G} usually doesn't have two distinct eigenvalues but three [70], they can be decomposed into generators that have only two distinct eigenvalues (for instance, Pauli strings P_x with eigenvalues ± 1) and the gradient can be directly calculated by the product rule and the parameter shift rule [70, 71], necessitating 2^{2n} expectation values. So even for a UCCD ansatz, we would need around $2^4 = 16$ expectation values for a single gradient calculation (to be multiplied by the number of parameters).

Turning to the Hessian estimation, one can derive Eq. (A13) with respect to another parameter θ_k ,

$$H_{kj}^{CC} = \frac{1}{2} \sum_n^{\forall P_n \in \mathcal{G}_j} \left(\frac{\partial}{\partial \theta_k} \langle \hat{\mathcal{M}} \rangle_{\theta_{j_n}^+} - \frac{\partial}{\partial \theta_k} \langle \hat{\mathcal{M}} \rangle_{\theta_{j_n}^-} \right) \tag{A15}$$

and use the parameter-shift rule again, thus leading to [66]

$$\begin{aligned}
H_{kj}^{CC} &= \frac{1}{4} \sum_n^{\forall P_n \in \mathcal{G}_j} \sum_m^{\forall P_m \in \mathcal{G}_k} \left(\langle \hat{\mathcal{M}} \rangle_{\theta_{j_n}^+ \theta_{k_m}^+} - \langle \hat{\mathcal{M}} \rangle_{\theta_{j_n}^+ \theta_{k_m}^-} \right. \\
&\quad \left. - \langle \hat{\mathcal{M}} \rangle_{\theta_{j_n}^- \theta_{k_m}^+} + \langle \hat{\mathcal{M}} \rangle_{\theta_{j_n}^- \theta_{k_m}^-} \right).
\end{aligned} \tag{A16}$$

According to Eq. (A16), a single element of the Hessian will require the estimation of 2^{4n} expectation values for a n -fold fermionic excitation operator.

Different strategies have recently been developed to reduce the number of expectation values required to evaluate a circuit-parameter gradient of a fermionic generator \mathcal{G} with more than two distinct eigenvalues. One

can consider an additional ancilla qubit and decompose the derivative into a linear combination of unitaries [65], use stochastic strategies [72, 73] or different generator decomposition techniques [70, 74].

Appendix B: Orbital gradient \mathbf{G}^O and Hessian \mathbf{H}^{OO}

In this appendix, we show how the orbital gradient and Hessian can be estimated from the one- and two-particle reduced density matrices (1-RDM and 2-RDM) that are measured out of the quantum circuit. For simplicity, let us focus on single wavefunction $|\Psi_I(\boldsymbol{\theta})\rangle$ for which we want to optimize the orbitals. The generalization to a weighted-ensemble of state (as in SA-OO-VQE) is straightforward, as one just has to replace the state-specific 1- and 2-RDMs by the state-averaged 1- and 2-RDMs. The parametrized energy of the state reads

$$E_I(\boldsymbol{\kappa}, \boldsymbol{\theta}) = \langle \Psi_I(\boldsymbol{\theta}) | \hat{U}_O(\boldsymbol{\kappa})^\dagger \hat{\mathcal{H}} \hat{U}_O(\boldsymbol{\kappa}) | \Psi_I(\boldsymbol{\theta}) \rangle, \quad (\text{B1})$$

where the orbital rotation operator is defined such that

$$\hat{U}_O(\boldsymbol{\kappa}) = e^{-\hat{\kappa}}, \text{ with } \hat{\kappa} = \sum_{p>q} \kappa_{pq} \hat{E}_{pq}^-. \quad (\text{B2})$$

with $\hat{E}_{pq}^- = \hat{E}_{pq} - \hat{E}_{qp}$. Expanding to second order in $\boldsymbol{\kappa}$ the operator $\hat{U}_O(\boldsymbol{\kappa})^\dagger \hat{\mathcal{H}} \hat{U}_O(\boldsymbol{\kappa})$ leads to

$$E_I(\boldsymbol{\kappa}, \boldsymbol{\theta}) \simeq \langle \Psi_I(\boldsymbol{\theta}) | \left(\hat{\mathcal{H}} + [\hat{\kappa}, \hat{\mathcal{H}}] + \frac{1}{2} [\hat{\kappa}, [\hat{\kappa}, \hat{\mathcal{H}}]] \right) | \Psi_I(\boldsymbol{\theta}) \rangle, \quad (\text{B3})$$

which, when compared to the second-order Taylor expansion of $E_I(\boldsymbol{\kappa})$ with respect to the $\boldsymbol{\kappa}$ parameters,

$$E_I(\boldsymbol{\kappa}, \boldsymbol{\theta}) \simeq E_I(0, \boldsymbol{\theta}) + \boldsymbol{\kappa}^\dagger \mathbf{G}^{O,I} + \frac{1}{2} \boldsymbol{\kappa}^\dagger \mathbf{H}^{OO,I} \boldsymbol{\kappa}, \quad (\text{B4})$$

allows to identify the MO-gradient and MO-Hessian elements, defined as follows:

$$G_{pq}^{O,I} = \frac{\partial E_I}{\partial \kappa_{pq}} = \langle \Psi_I(\boldsymbol{\theta}) | [\hat{E}_{pq}^-, \hat{\mathcal{H}}] | \Psi_I(\boldsymbol{\theta}) \rangle \quad (\text{B5})$$

for the gradient, and

$$\begin{aligned} H_{pq,rs}^{OO,I} &= \frac{\partial^2 E_I}{\partial \kappa_{pq} \partial \kappa_{rs}} \\ &= \frac{1}{2} \left(1 + \mathcal{S}_{(pq)}^{(rs)} \right) \langle \Psi_I(\boldsymbol{\theta}) | [\hat{E}_{pq}^-, [\hat{E}_{rs}^-, \hat{\mathcal{H}}]] | \Psi_I(\boldsymbol{\theta}) \rangle \end{aligned} \quad (\text{B6})$$

for the Hessian, where $\mathcal{S}_{(pq)}^{(rs)}$ is an operator that permutes the two couples of indices (pq) and (rs) . In practice, one can derive an analytic form of the orbital gradient and Hessian based on the 1 and 2-RDMs and the electronic integrals. As this derivation is fastidious, we only introduce the final equations required for the implementation.

Starting with the orbital gradient $\mathbf{G}^{O,I}$, the elements of the associated matrix read

$$G_{pq}^{O,I} = 2(F_{pq}^I - F_{qp}^I), \quad (\text{B7})$$

where the elements of the generalized Fock matrix \mathbf{F}^I (associated to the state $|\Psi_I\rangle$) read

$$F_{pq}^I = \sum_t \gamma_{pt}^I h_{qt} + \sum_{t,u,v} \Gamma_{ptuv}^I g_{qtuv}. \quad (\text{B8})$$

In practice, building the full matrix can be very expensive. However and as described in Ref. 11, considering an active space partitioning does reduce this complexity considerably. In this partitioning, the Fock matrix is fragmented into three contributions:

$$F_{iq}^I = 2(F_{qi}^{\text{frozen},I} + F_{qi}^{\text{active},I}), \quad (\text{B9})$$

$$F_{vq}^I = \sum_w^{\text{active}} F_{qw}^{\text{frozen},I} \gamma_{vw}^I + \sum_{w,x,y}^{\text{active}} \Gamma_{vwxy}^I g_{qwxy}, \quad (\text{B10})$$

and

$$F_{aq}^I = 0, \quad (\text{B11})$$

where i, v and a refer to frozen occupied, active and virtual MOs, respectively, and $\mathbf{F}^{\text{frozen},I}$ and $\mathbf{F}^{\text{active},I}$ are the so-called frozen and active Fock matrices that read

$$F_{pq}^{\text{frozen},I} = h_{pq} + \sum_i^{\text{frozen}} (2g_{pqii} - g_{pii q}) \quad (\text{B12})$$

and

$$F_{pq}^{\text{active},I} = \sum_{w,x}^{\text{active}} \gamma_{wx}^I (g_{pqwx} - \frac{1}{2} g_{pxwq}). \quad (\text{B13})$$

Turning to the orbital Hessian $\mathbf{H}^{OO,I}$, the elements of the associated matrix read

$$\begin{aligned} H_{pq,rs}^{OO,I} &= (1 - \mathcal{S}_{pq})(1 - \mathcal{S}_{rs}) \left\{ (F_{ps}^I + F_{sp}^I) \delta_{qr} - 2h_{ps} \gamma_{qr}^I \right. \\ &\quad \left. + 2 \sum_{t,u} (g_{purv} (\Gamma_{qusv}^I + \Gamma_{quvs}^I) + g_{pruv} \Gamma_{qsuv}^I) \right\} \end{aligned} \quad (\text{B14})$$

where \mathcal{S}_{pq} (\mathcal{S}_{rs}) is an operator permuting the indices p and q (r and s).

Note that, within the active space approximation, only the 1- and 2-RDM elements from the active space have to be measured on the quantum computer. Every other non-zero terms of the RDMs read

$$\gamma_{ij}^I = \gamma_{ji}^I = 2\delta_{ij} \quad (\text{B15})$$

$$\Gamma_{ijkl}^I = 4\delta_{ij}\delta_{kl} - 2\delta_{il}\delta_{jk} \quad (\text{B16})$$

$$\Gamma_{ijwx}^I = \Gamma_{wxij}^I = 2\gamma_{wx}^I \delta_{ij} \quad (\text{B17})$$

$$\Gamma_{iwxj}^I = \Gamma_{xjiw}^I = -\gamma_{wx}^I \delta_{ij} \quad (\text{B18})$$

where i, j, k, l and w, x denote frozen and active MO indices, respectively.

Appendix C: Circuit-orbital hessian \mathbf{H}^{CO}

In practice, one can estimate the off-diagonal blocks of the Hessian matrix \mathbf{H}^{CO} by repeated measurements of the quantum circuit. From the definition of the molecular orbital gradient in Eq. (B5), one obtains

$$\begin{aligned} H_{j,pq}^{\text{CO},I} &= \frac{\partial}{\partial \theta_j} \frac{\partial E_I}{\partial \kappa_{pq}} \\ &= \frac{\partial}{\partial \theta_j} \langle \Psi_I(\boldsymbol{\theta}) | [\hat{E}_{pq}^-, \hat{\mathcal{H}}] | \Psi_I(\boldsymbol{\theta}) \rangle \\ &= \frac{\partial}{\partial \theta_j} \text{Tr} [\hat{\mathcal{M}} \hat{\rho}_I(\boldsymbol{\theta})], \end{aligned} \quad (\text{C1})$$

where $\hat{\rho}_I(\boldsymbol{\theta}) = |\Psi_I(\boldsymbol{\theta})\rangle \langle \Psi_I(\boldsymbol{\theta})|$ and $\hat{\mathcal{M}} = [\hat{E}_{pq}^-, \hat{\mathcal{H}}]$. Using the parameter-shift rule on the operator $\hat{\mathcal{M}}$ (see Appendix A), we obtain the elements of $\mathbf{H}^{\text{CO},I}$ as

$$H_{j,pq}^{\text{CO},I} = \frac{1}{2} \sum_n^{\forall P_n \in \mathcal{G}_j} \left(\langle \hat{\mathcal{M}} \rangle_{\theta_{jn}^+} - \langle \hat{\mathcal{M}} \rangle_{\theta_{jn}^-} \right). \quad (\text{C2})$$

According to Eq. (C2), one can measure the expectation values of the new operator $\hat{\mathcal{M}} = [\hat{E}_{pq}^-, \hat{\mathcal{H}}]$, with the appropriate shift-in-parameter defined from the parameter-shift rule. In practice, Eq. (C2) can be rewritten in terms of generalized Fock matrices,

$$H_{j,pq}^{\text{CO},I} = \sum_n^{\forall P_n \in \mathcal{G}_j} \left(F_{\theta_{jn}^+, pq}^I - F_{\theta_{jn}^+, qp}^I - F_{\theta_{jn}^-, pq}^I + F_{\theta_{jn}^-, qp}^I \right), \quad (\text{C3})$$

which elements can be computed according to Eq. (B8), with the 1- and 2-RDMs associated to the θ_{jn}^\pm -shifted state. The elements of the opposite off-diagonal Hessian block are simply built based on the symmetry $\mathbf{H}^{\text{CO}} = (\mathbf{H}^{\text{CO}})^T$.

Appendix D: Nuclear derivative of the electronic Hamiltonian operator

In the coupled-perturbed equations, one needs the derivative of the Hamiltonian operator with respect to a nuclear coordinate [20, 46, 75, 76] which is defined by

$$\frac{\partial \hat{\mathcal{H}}}{\partial x} = \sum_{p,q} \frac{\partial h_{pq}}{\partial x} \hat{E}_{pq} + \frac{1}{2} \sum_{p,q,r,s} \frac{\partial g_{pqrs}}{\partial x} \hat{e}_{pqrs} + \frac{\partial E_{\text{nuc}}}{\partial x}, \quad (\text{D1})$$

where the derivative of the electronic integrals are

$$\frac{\partial h_{pq}}{\partial x} = h_{pq}^{(x)} - \frac{1}{2} \left\{ S^{(x)}, h \right\}_{pq} \quad (\text{D2})$$

$$\frac{\partial g_{pqrs}}{\partial x} = g_{pqrs}^{(x)} - \frac{1}{2} \left\{ S^{(x)}, g \right\}_{pqrs} \quad (\text{D3})$$

where we retrieve ‘explicit’ and ‘response’ terms with respect to a nuclear coordinate. The explicit terms are the ones super-scripted with $^{(x)}$ indicating a differentiation of the primitive atomic orbitals (MOs coefficients remaining constant). They are defined such as

$$S_{pq}^{(x)} = \sum_{\mu, \nu}^{\text{AOs}} C_{\mu p} C_{\nu q} \frac{\partial S_{\mu\nu}}{\partial x} \quad (\text{D4})$$

$$h_{pq}^{(x)} = \sum_{\mu, \nu}^{\text{AOs}} C_{\mu p} C_{\nu q} \frac{\partial h_{\mu\nu}}{\partial x} \quad (\text{D5})$$

$$g_{pqrs}^{(x)} = \sum_{\mu, \nu, \delta, \gamma}^{\text{AOs}} C_{\mu p} C_{\nu q} C_{\delta r} C_{\gamma s} \frac{\partial g_{\mu\nu\delta\gamma}}{\partial x} \quad (\text{D6})$$

where \mathbf{C} is the MO coefficient matrix encoding the optimal orbitals that minimize the state-averaged energy. The ‘response’ terms in curly bracket are defined as

$$\left\{ S^{(x)}, h \right\}_{pq} = \sum_o \left(S_{po}^{(x)} h_{oq} + S_{qo}^{(x)} h_{po} \right) \quad (\text{D7})$$

$$\left\{ S^{(x)}, g \right\}_{pqrs} = \sum_o \left(S_{po}^{(x)} g_{oqrs} + S_{qo}^{(x)} g_{pors} \right) \quad (\text{D8})$$

$$+ S_{ro}^{(x)} g_{pqos} + S_{so}^{(x)} g_{pqro}. \quad (\text{D9})$$

The last term present on the right of Eq. D1 is the nuclear derivative of the nuclear repulsion energy which is pretty straightforward to compute in practice.